

Structural, Dielectric, Magnetic and Magneto-Dielectric Properties of $(1-x)\text{BiFeO}_3-(x)\text{CaTiO}_3$ Composites

Bushra Khan

Centre of Material Science, University of Allahabad

Aditya Kumar

Centre of Material Science, University of Allahabad

Preeti Yadav

Allahabad University: University of Allahabad

Gulab Singh

Centre of Material Sciences, University of Allahabad

Ashok Kumar

National Physical Laboratory CSIR New Delhi

Manoj Kumar Singh (✉ mksingh100@yahoo.com)

Centre of Material Science, University of Allahabad <https://orcid.org/0000-0002-8122-7279>

Research Article

Keywords: Multiferroic, Activation Energy, Ferromagnetic and Magneto-dielectric coupling

Posted Date: March 11th, 2021

DOI: <https://doi.org/10.21203/rs.3.rs-272797/v1>

License:   This work is licensed under a Creative Commons Attribution 4.0 International License.

[Read Full License](#)

Structural, dielectric, magnetic and magneto-dielectric properties of (1-x)BiFeO₃-(x)CaTiO₃ composites

Bushra Khan¹, Aditya Kumar¹, PreetiYadav¹, Gulab Singh¹, Ashok Kumar², Manoj K. Singh^{1*}

¹Center of Material Sciences, Institute of Interdisciplinary Studies (IIDS), University of Allahabad, Allahabad-211002, India

²National Physical Laboratory (CSIR), New Delhi -110012, India

ABSTRACT

(1-x) BiFeO₃-(x) CaTiO₃ [(1-x) BFO – (x) CTO, (x=0, 0.1, 0.2 and 0.3)] composites were synthesized using sol-gel chemical rout method. X-ray diffraction investigation shows the crystal structure changes from rhombohedral to monoclinic for $0 \leq x \leq 0.2$, and it changes to orthorhombic at $x \leq 0.3$. The Field Emission Scanning Electron Microscope (FESEM) investigation confirms the the microstructure consists of randomly oriented, homogenous, and non-uniform grains. The dielectric permittivity (ϵ) and tangent loss ($\tan\delta$) decreases with increasing frequency and show dielectric anomalies (as a hump) at different temperatures for different compositions. The incorporation of CTO, decreases three order of leakage current (up to $x=0.2$) and significantly improve the magnetization and magneto-dielectric coupling. The frequency-dependent ac conductivity obeys Jonscher's power law with large ac conductivity dispersion for higher frequencies with increasing CTO concentration. The variations of ac conductivity with the inverse of temperature obey the Arrhenius equation and show negative temperature coefficient of resistance (NTCR) behavior. The ferromagnetic (FM) properties in BFO-CTO increases significantly with an increase of the CTO concentration. The coercive field increases with increasing CTO concentration suggesting a competition between the antiferromagnetic and ferromagnetic ordering. At room temperature, all the samples show strong magneto-dielectric coupling.

Keywords: Multiferroic, Activation Energy, Ferromagnetic and Magneto-dielectric coupling.

*Email of corresponding authors: mksingh100@allduniv.ac.in.

1 Introduction

Researchers have attracted multiferroic materials in this current scientific age due to their vital applications in magnetic sensors, multiple state memories, data exhibiting storage devices, spintronics, energy conversion, and energy harvesting devices [1,2]. These materials possess two or more ferroic features such as ferromagnetism, ferroelectricity, or ferroelasticity effects. The multiferroic materials have the potential of exhibiting magneto-electric coupling effect (ME), inducing magnetic (electric) polarization by applying an external electric (magnetic) field [3-6]. The single crystal shows a weak ME effect due to the mechanism of ferroelectricity and magnetism being very different and often contradictory, and these materials are hardly used for device application due to temperature restraint [7]. These problems can be overcome by the synthesis of composites and solid solutions of ferroelectric and ferrite components [8-11].

BiFeO_3 - ABO_3 type composite solid solutions/compounds have recently concerned universal consideration due to their attractive electric and magnetic properties [11, 12]. Bismuth Ferrite (BiFeO_3) is an attractive material that exhibit multiferroic properties at room temperature, which is ferroelectric ($T_C \sim 1103$ K) and antiferromagnetic ($T_N \sim 643$ K) [13-20]. BiFeO_3 (BFO) is an inorganic chemical compound having a perovskite structure with space group $R3c$. The ferroelectricity arises due to the displacement of Bi^{3+} and Fe^{3+} cations along the [111] threefold polar and the existence of weak ferromagnetism is due to the G type canted spins antiferromagnetic structure [21]. The creation of oxygen vacancies and the valence fluctuation of iron ions, i.e. $\text{Fe}^{3+} / \text{Fe}^{2+}$, cause poor resistivity in BFO. Another major drawback of BiFeO_3 material is the leakage current arising out of its non-stoichiometry. These deficiencies of BFO can be overcome by introducing ABO_3 type perovskites like BaTiO_3 , SrTiO_3 , PbTiO_3 , CaTiO_3 , etc form solid solutions because one can expect that these materials improve the multiferroic properties [22-23].

The quantum paraelectric (or incipient ferroelectrics) such as SrTiO_3 , KTiO_3 , and CaTiO_3 [22] have been attracted huge attention due to their polar soft modes but do not show a ferroelectric phase transition (T_C) as the temperature goes down to zero Kelvin. The ferroelectric and quantum fluctuations are supposed to contend with each other in them [23]. CaTiO_3 exhibits an orthorhombic structure with space group Pbnm up to 1380K, and it belongs to another space group Cmcm of the same structure between 1380 and 1500K [24]. At 1500K, it changes from orthorhombic (Cmcm) to tetragonal ($I4/m\bar{c}m$), and it becomes cubic ($\text{Pm}\bar{3}m$) with further increasing the temperature. According to V.V. Lemanov et. al. [22] and others [23,24], CaTiO_3 has quantum paraelectric similar to SrTiO_3 or KTiO_3 or an classified incipient ferroelectric because of their similar dielectric behaviour i.e. high dielectric permittivity which can be saturated at low temperature and also shows large and negative value of temperature coefficient ($d\epsilon/dT$) [22-24].

In the present work, $(1-x)\text{BiFeO}_3 - x\text{CaTiO}_3$ [$0 \leq x \leq 0.3$] composite solid solutions were synthesized by using the sol-gel method. The dielectric properties have been investigated in the frequency range of 1 kHz to 1MHz from temperature 300K to 700K. We observed that the electrical, magnetic, and magneto-dielectric properties are significantly increased in composites compared to pure BFO.

2 Experimental

The $(1-x)$ BFO – (x) CTO, ($x=0, 0.1, 0.2$ and 0.3) multiferroic composite was prepared by using the sol-gel method. For the preparation of the precursor solution, bismuth nitrate pentahydrate [AlfaAesar], iron nitrate nonahydrate [AlfaAesar], calcium carbonate [AlfaAesar], titanium isopropoxide [AlfaAesar], ethylene glycol

and 2-methoxy ethanol were used as a solvent. Nitric acid and acetic acid used as a catalyst. The precise quantities of ethylene glycol and 2-methoxy ethanol were mixed and stirred to attain homogenization. Bismuth nitrate (5 mol% excess because of bismuth evaporation at high temperature), iron nitrate, and calcium carbonate were dissolved separately in the prepared solvent. Acetic acid and nitric acid was added during the reaction process. After complete dissolution of all precursors, they mixed together to form Bi-Fe-Ca solution. In a separate beaker, a solution of 2-methoxy ethanol and acetylacetone was prepared, and titanium isopropoxide was incorporated in that prepared solution. This Ti solution was added to Bi-Fe-Ca solution to form the (1-x) BFO – (x) CTO precursor. The solutions were heated at 373K with continuous stirring for 24 hours to form gel. The obtained gels of different BFO and CTO compositions were dried and calcined at 1093K for 4 hours. Finally, palettes of (1-x) BFO – (x)CTO were prepared and sintered for 6 hour at 1073K. For electrical measurements, palettes were coated by conducting silver and dried at 473K for two hours.

The synthesized sample's structural properties were investigated by using the X-ray diffraction (XRD) [RigakuMiniflex-II X-ray diffract meter] using wavelength of 1.506 Å and CuK α radiation. The Field Emission Scanning Electron Microscope (FESEM, FEI Quanta 400) was used to study the surface morphology of the synthesized samples. The dielectric measurements were carried out using Nova control Alpha-A high-performance Frequency Analyser in the frequency range from 1kHz to 1MHz, and temperature-dependent dielectric measurements were recorded in the range of 300K to 673K. The magnetic properties (M-H curve) of samples were recorded by PPMS VERSALAB vibrating sample magnetometer (VSM). Magneto - dielectric effect in these samples were measured at 300K using Nova control under a varying magnetic field up to 1.0 Tesla.

3 Results and discussion

3.1 Structural Analysis

Fig. 1 shows the X-ray diffraction (XRD) pattern of (1-x)BiFeO₃ - (x)CaTiO₃ for x = 0.0, 0.1, 0.2 and 0.3. The XRD pattern is in good agreement with the rhombohedral perovskite structure with space group *R3c* for pure BFO. All the observed diffraction peaks of BiFeO₃ and CaTiO₃ are indexed by using JCPDS Card No: 74-2493 and 78-1013, respectively. A secondary phase of impurity peak at ~27.6° was observed only in BFO, possibly associated with the impurity phase of Bi₂Fe₄O₉ due to the highly volatile nature of bismuth [25, 26], and this secondary phase did not observe as the CTO concentration increases [26]. Fig. 1 also reveals that all the XRD peaks associated with BFO shifted to a higher angle side, whereas each peak's intensity decreases with increasing CTO concentration.

The enlarged portion of the XRD diffraction peaks at (010), (110) and (111) are presented in Fig. 2 (a), (b), and (c), respectively for (1-x) BFO – (x) CTO samples. Fig. 2(a) shows that the peak (010) is shifted towards the higher angle side with increasing CTO content and split into two different peaks for x=0.3. From Fig. 2(b) and 2(c), it is observed that the diffraction peaks at (110) and ($\bar{1}$ 10) are merged into one peak for x= 0.1 and 0.2 and again splitted into two different peaks with noticeable shifting towards higher angle side. A similar result was observed for the diffraction peaks at (111) and ($\bar{1}$ 11) in Fig. 2(c). These observations reveal that the shifting towards the higher angle side with an increase in CTO composition may be due to the substitution of Ca²⁺ and Ti⁴⁺ ions on Bi³⁺ and Fe³⁺ ions in BFO lattice, respectively.

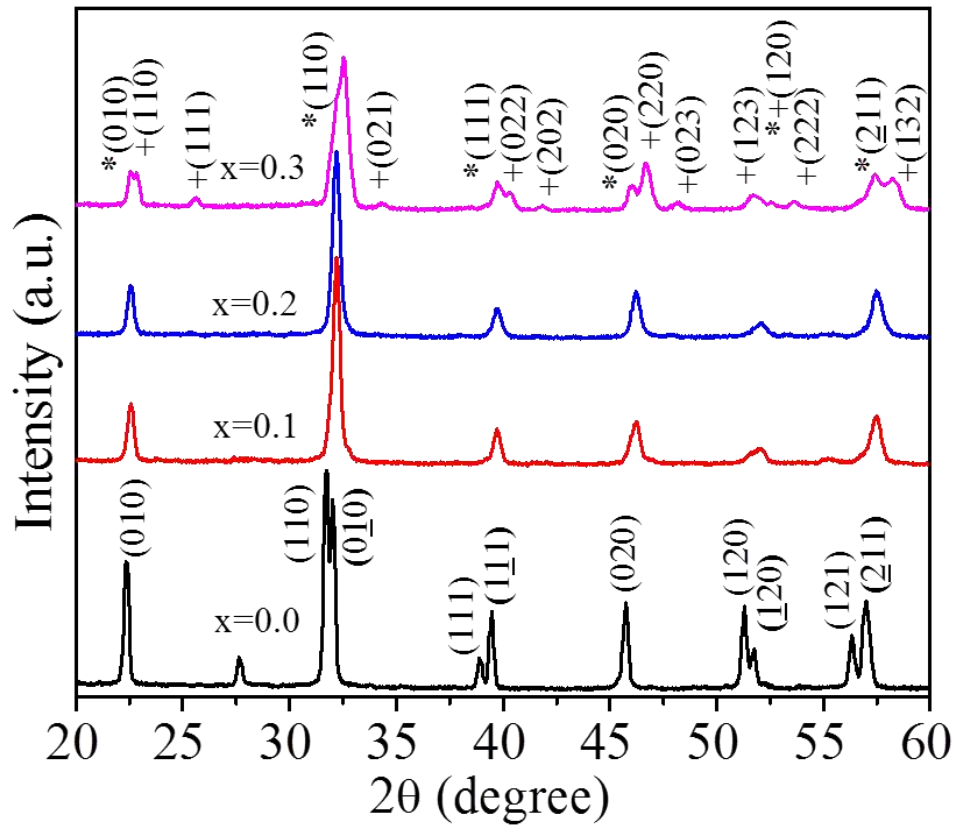


Fig. 1 X- ray diffraction (XRD) pattern of $(1-x)$ BFO- (x) CTO [$x=0, 0.1, 0.2$ and 0.3] , where (+) denotes ferrite phase and (*) denotes the ferroelectric phase.

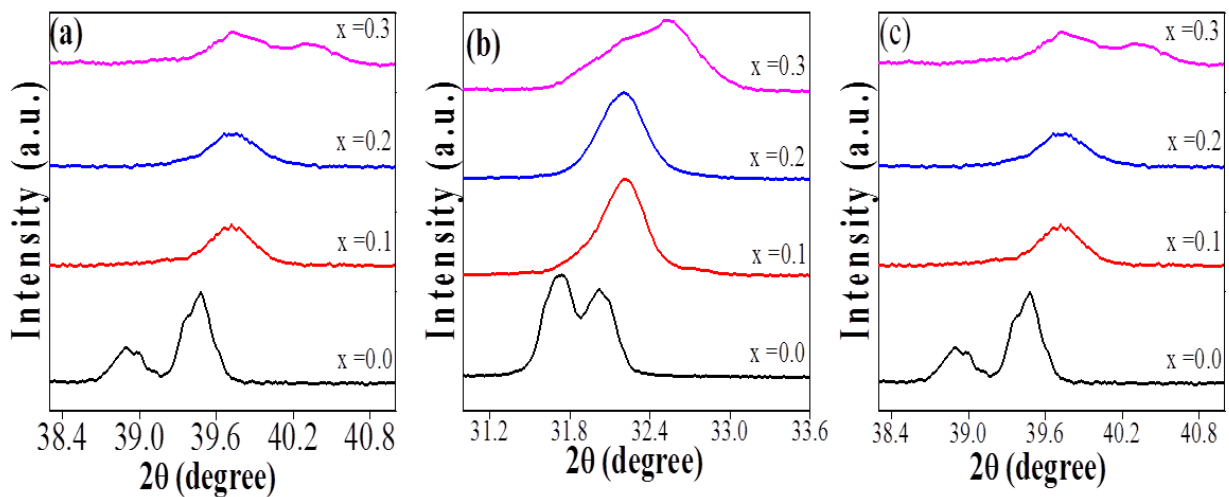


Fig. 2 Zoom XRD pattern of $(1-x)$ BFO- (x) CTO [$x=0, 0.1, 0.2$ and 0.3] to show the peak shifting by enlarge the peaks in 2θ range.

Also, the size of the ions Ca^{2+} (1.06\AA) and Ti^{4+} (0.61\AA) are smaller than the Bi^{3+} (1.17\AA) and Fe^{3+} (0.65\AA) ions, which may change the lattice constant of BFO lattice. The occurrence of double peaks at $x=0$, indicates the lower symmetry crystal structure, and this is the predominant characteristic of the rhombohedral

structure. The non-appearance of double peaks for $x=0.1$ and 0.2 indicates the occurrence of the crystal structure of advanced symmetry, i.e., the doublet peaks overlap to provide a single peak, which is a typical reflection of the monoclinic phase. The asymmetric broadening for $x=0.3$ confirms the occurrence of a lower symmetry crystal structure. The former major changes are observed in XRD patterns for $x=0.3$, such as the promising new reflections [marked by the symbol (+) in Fig.1], which are absent for $x=0.1$ and 0.2 . Thus, we predict that for pure BFO ($x=0$), the crystal structure should be rhombohedral (space group $R3c$) while for $x=0.1$ and $x=0.2$, it should be the monoclinic phase (space group Cc), and for $x=0.3$ samples, the crystal structure should be orthorhombic (space group $Pbnm$). These observed structural changes in samples are consistent with an earlier report presented in Ref 27, 28. It can be concluded that the concentration range can expand the structural stability of the polar rhombohedral phase by co-doping with Ca^{2+} and Ti^{4+} ions[28, 29]. The concentration phase transition from polar to non-polar orthorhombic phase is another essential difference of the Ca/Ti doping approach.

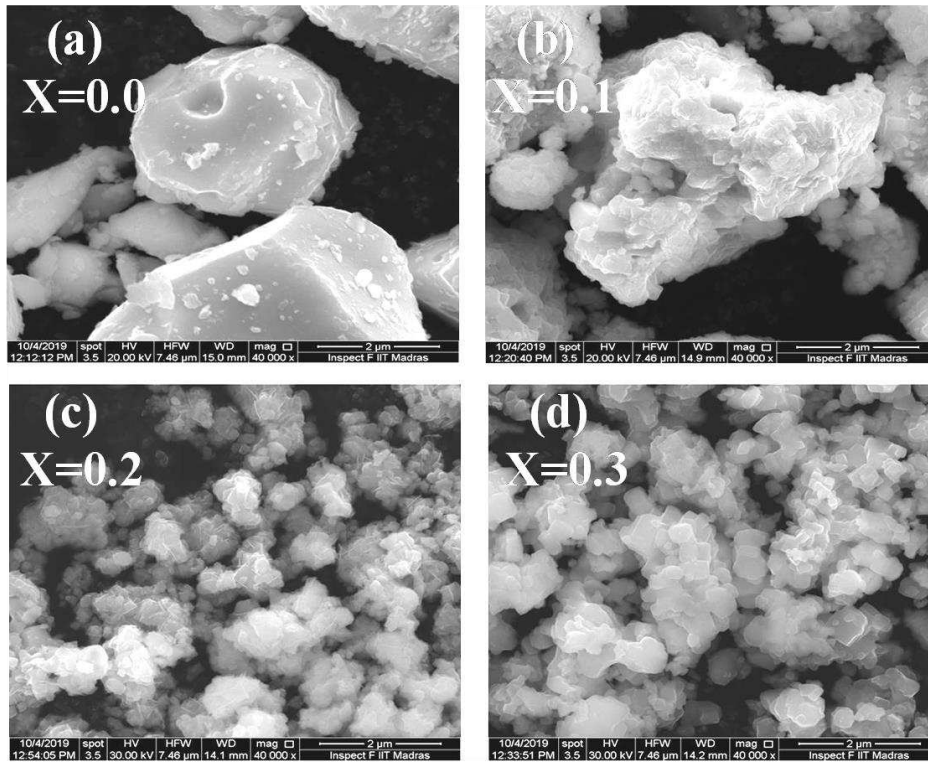


Fig.3 Surface morphology of the $(1-x)BFO - (x)CTO$ [$x=0, 0.1, 0.2$ and 0.3]

The FESEM micrograph for $(1-x) BFO - (x) CTO$ is shown in Fig. 3, and reveals that the microstructure consists of randomly oriented, homogenous, and non-uniform grains. It is also confirmed that the grains become more compact with increasing CTO content. Also, the size of grains decreases upto $x=0.2$ and after that, it increases. This may be due to structural change from monoclinic to orthorhombic.

3.2 Dielectric properties

Fig.4(a) to 4(d) show the change of dielectric permittivity (ϵ) with frequency (1kHz to 1MHz) at selected temperature for $(1-x)BFO - (x)CTO$ [$x=0, 0.1, 0.2$ and 0.3], respectively. The dielectric permittivity decreases monotonically with increasing frequencies for all the compositions. The low-frequency dispersion

may be recognized due to space charge formation causing interfacial polarization due to the A-site vacancies [30], whereas, at high frequencies, these space charges find very little time to make up and thus incapable of experiencing the relaxation process [31]. All the samples show dispersion in a low-frequency region, which can be explained by Maxwell Wagner type interfacial polarization [32, 33]. Further, a substantial increase in dielectric permittivity (ϵ) in the low-frequency range may be due to the additional contribution of dipolar polarization, which shows the temperature-dependent dielectric permittivity behaviour [34].

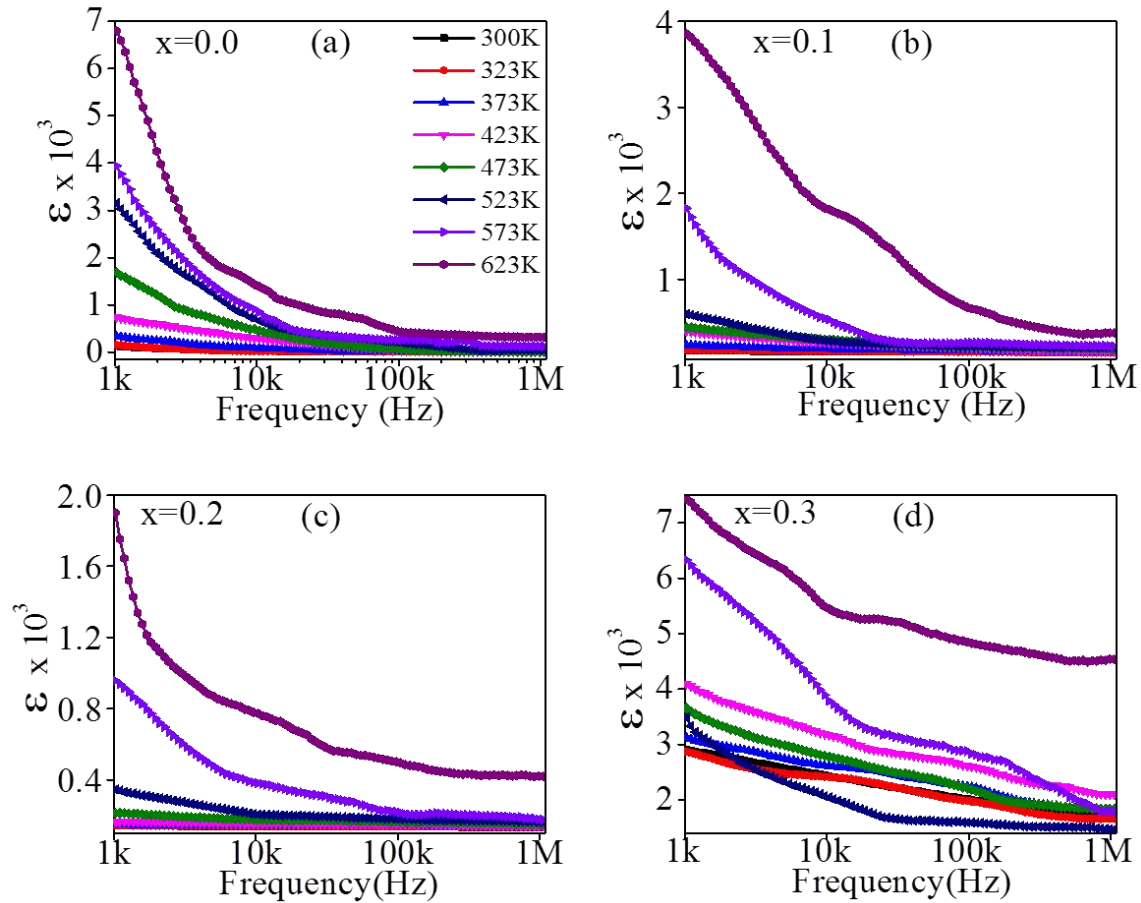


Fig. 4 Frequency dependence of dielectric permittivity (ϵ) at selected temperature for $(1-x)\text{BFO} - (x)\text{CTO}$ [$x=0, 0.1, 0.2$ and 0.3]

Dipolar and interfacial polarization do not contribute at higher frequency regions that resulted in a decrease in dielectric permittivity and almost become constant, and it can be explained by the dipolar relaxation phenomenon [31]. All the samples show dispersion [32, 33], which is in good concurrence with Koop's phenomenological theory as the dipoles require some time to align themselves in the direction of the applied field because, in the dielectric medium, they do not instantly act in response to the applied field [35]. As the frequency increases to a certain point, the dielectric medium's charge carriers do not precisely follow the applied frequency; therefore, the value of dielectric permittivity (ϵ) decreases. This may be due to the hopping mechanism of electrons from Fe^{2+} to Fe^{3+} ions [36].

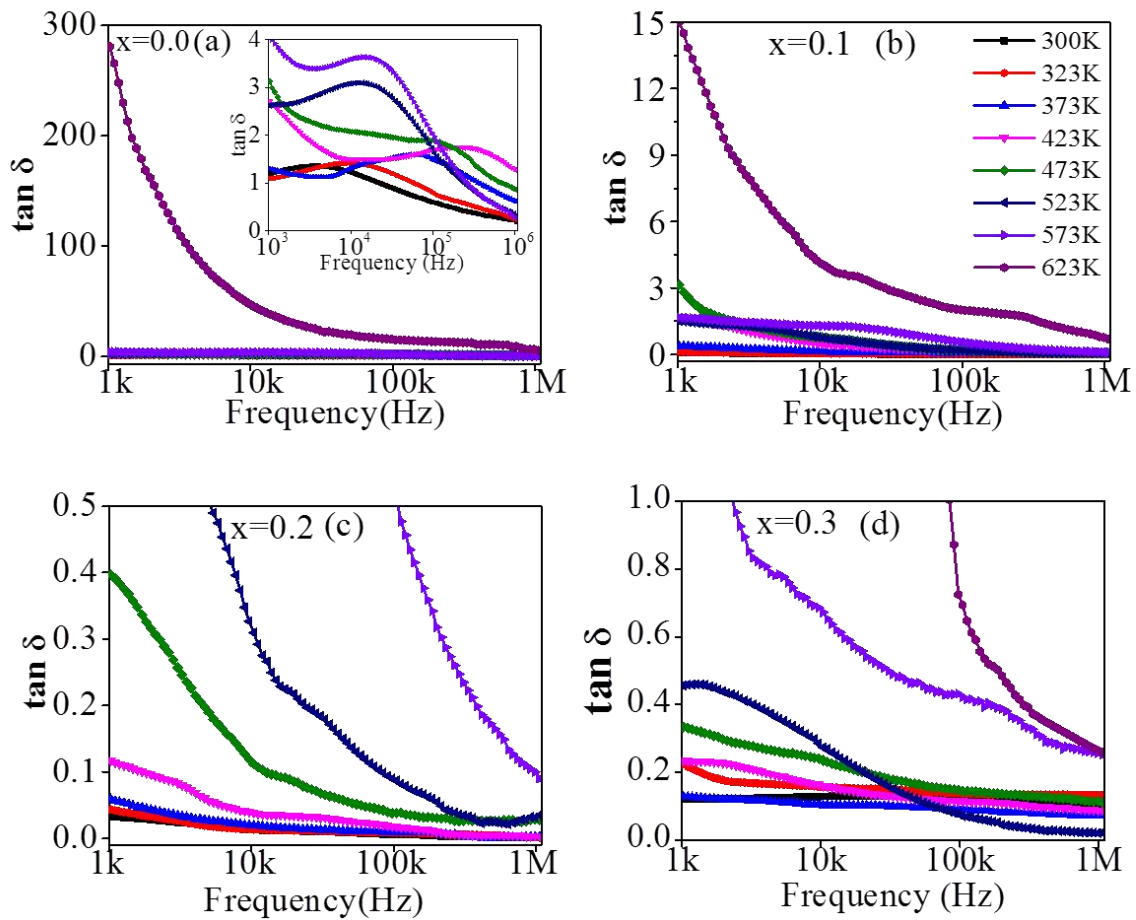


Fig. 5 Frequency dependence of tangent loss ($\tan\delta$) at selected temperature for $(1-x)\text{BFO} - (x)\text{CTO}$ [$x=0, 0.1, 0.2$ and 0.3]

The tangent loss ($\tan\delta$) as a function of frequency (from 1kHz to 1MHz) are shown in Fig.5 (a) to 5(d) for the $(1-x)\text{BFO} - (x)\text{CTO}$ [$x=0.0, 0.1, 0.2$ and 0.3] samples at selected temperatures, respectively. It is observed that the tangent loss decreases with an increase in frequency from 1 kHz to 1MHz for all the synthesized samples. From Fig. 5, we also observed that the $\tan\delta$ of all the synthesized samples increase rapidly with an increase in temperature from 300 K to 620 K. A maxima has been observed in low-frequency range [shows in the inset of Fig. 5(a)], and its presence can be thought of the hopping frequencies of the electrons between different ionic states. A similar type of maxima has been previously reported in other multiferroic composites [37]. The dielectric losses ($\tan\delta$) are reduced at higher frequencies because it is related to the dissipation of energy in dielectric systems. The values of $\tan\delta$ for all samples are found much lower than that as compared to pure BFO samples, and its value is found to be minimum for $x=0.2$ composition.

The temperature dependence of dielectric permittivity and tangent loss ($\tan\delta$) at different frequencies (1kHz, 10kHz, 100kHz, and 1MHz) is plotted in Fig.6 and Fig. 7 for $x=0, 0.1, 0.2$ and 0.3 , respectively. In Fig. 6(a), the dielectric permittivity increases at a very slow rate in the low-temperature range [300K to 373K] and as temperature further increases the dielectric permittivity increases with a peak centered around the 640 K (close to T_N of BFO). This may be due to the participation of thermally activated dipoles. An anomalous change in

dielectric permittivity and tangent loss near 640 K (phase transition from antiferromagnetic to paramagnetic in pure BiFeO₃ sample) may be associated with the magneto-dielectric effect in the synthesized samples [13-20].

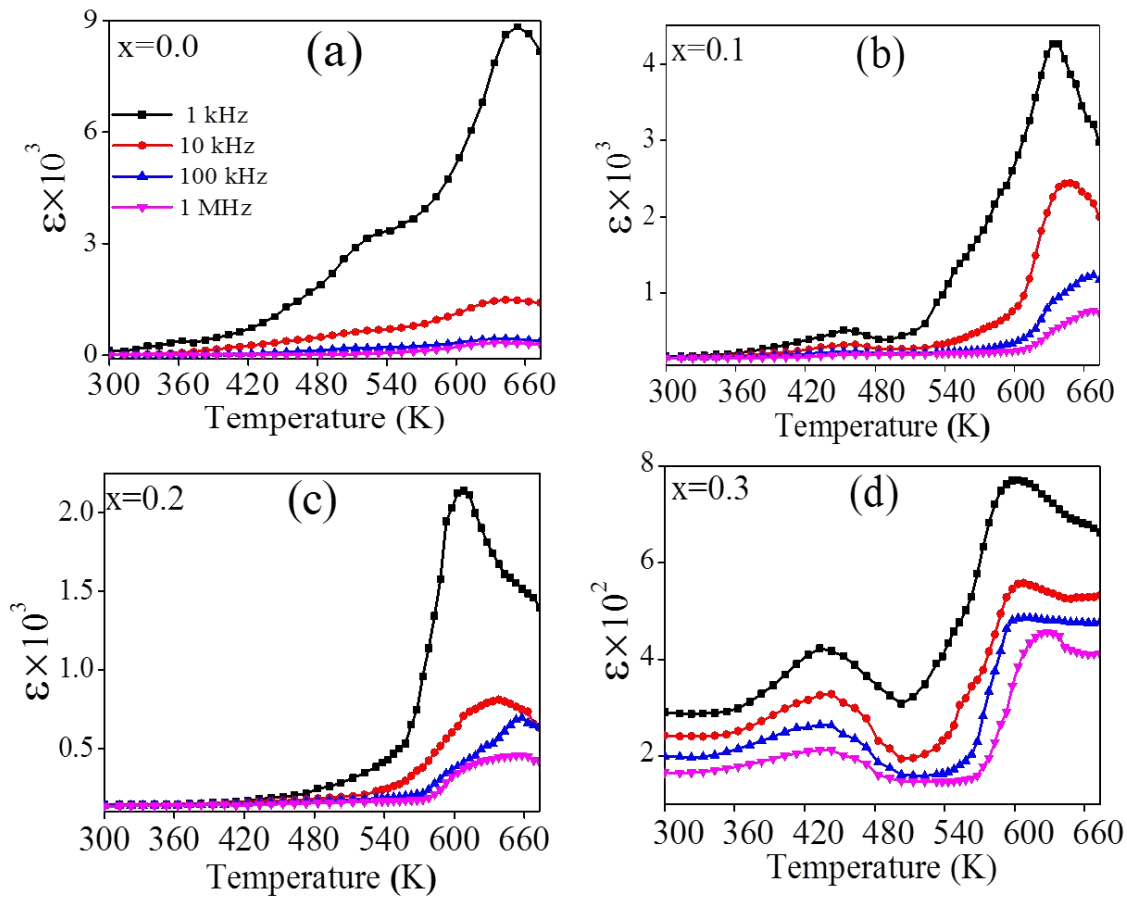


Fig. 6 Temperature dependence of dielectric permittivity (ϵ) at different frequencies for $(1-x)\text{BFO} - (x)\text{CTO}$ [$x=0, 0.1, 0.2$ and 0.3]

In Fig. 6(b, c, and d), we observed two anomalies peaks at $\sim 453\text{K}$ and $\sim 638\text{K}$ for $x=0.1$ and at $\sim 443\text{K}$ and $\sim 603\text{K}$ for $x=0.3$, whereas only second peak was observed at $\sim 608\text{K}$ for $x=0.2$. These peaks position shifted towards the higher temperature as frequencies increases from 1kHz to 1MHz . The observed anomaly near 453K and 443K in $0.9\text{BFO}-0.1\text{CTO}$ and $0.7\text{BFO}-0.3\text{CTO}$, respectively, can be described on the basis of the creation of defect through sintering at high temperature, which results in arising the defect dipoles inside the materials, and these defect dipoles relax due to applied temperature at different frequencies. With increasing frequencies, the hump (peak intensity) gets reduced because the defect dipoles cannot rotate at high frequencies [38]. These defects cannot be seen in $0.8\text{BFO}-0.2\text{CTO}$ because of its structural properties, which can be cleared by J-E characteristic. The leakage current measured in it to be lowest because of the absence of these defects. The second anomaly may be attributed due to the antiferromagnetic to paramagnetic transition ' T_N ' of BFO. The observed anomaly in dielectric dispersion with frequency and temperature near the Neel temperature (antiferromagnetic–paramagnetic phase transition temperature, T_N) suggests a strong coupling between magnetic and electric order parameters anomalies can be described by Landau-Devonshire theory of phase transition [39-41]. These anomalies in the dielectric permittivity (or loss) near the magnetic phase transition can

be attributed to the magneto-dielectric coupling effect [42, 43]. In $(1-x)\text{BFO} - (x)\text{CTO}$ [$x=0, 0.1, 0.2$ and 0.3] samples, as the Ti^{4+} concentration increases, the Fe^{2+} ions decreases, and the net oxygen vacancies reduce too in order to maintain of charge balance. This may be the probable reason of the decrease in magnetic phase transition temperature as the CTO concentration increases, as observed in Fig. 5 [44]. Fig. 6 shows that the observed anomalies shifted towards higher temperature side with increasing frequency for all the samples, and such type of behaviour may be due to the Maxwell Wagner type polarization arising from the heterogeneities in samples [32, 33]. All samples show different transition temperatures, and also it decreases with increment in CTO concentration due to compositional fluctuations occurring by the replacement of Bi^{3+} and Fe^{3+} by Ca^{2+} and Ti^{4+} dopants [45, 46].

The tangent loss ($\tan \delta$) increases with increasing temperature and shows the anomalous change near the magnetic phase transition temperature for all the compositions, as shown in Fig. 7. The rapid change in tangent loss near and above the transition temperature may be due to a change in the concentration of oxygen vacancies [47] and also due to the occurrence of extrinsic n-type conduction process in the samples due to Bi^{3+} and Ti^{4+} ions, as they act like a donor centers [47]. In addition, space charge polarization in BFO-CTO samples may also be the origin of a quick increase in $\tan \delta$ at high temperature [48].

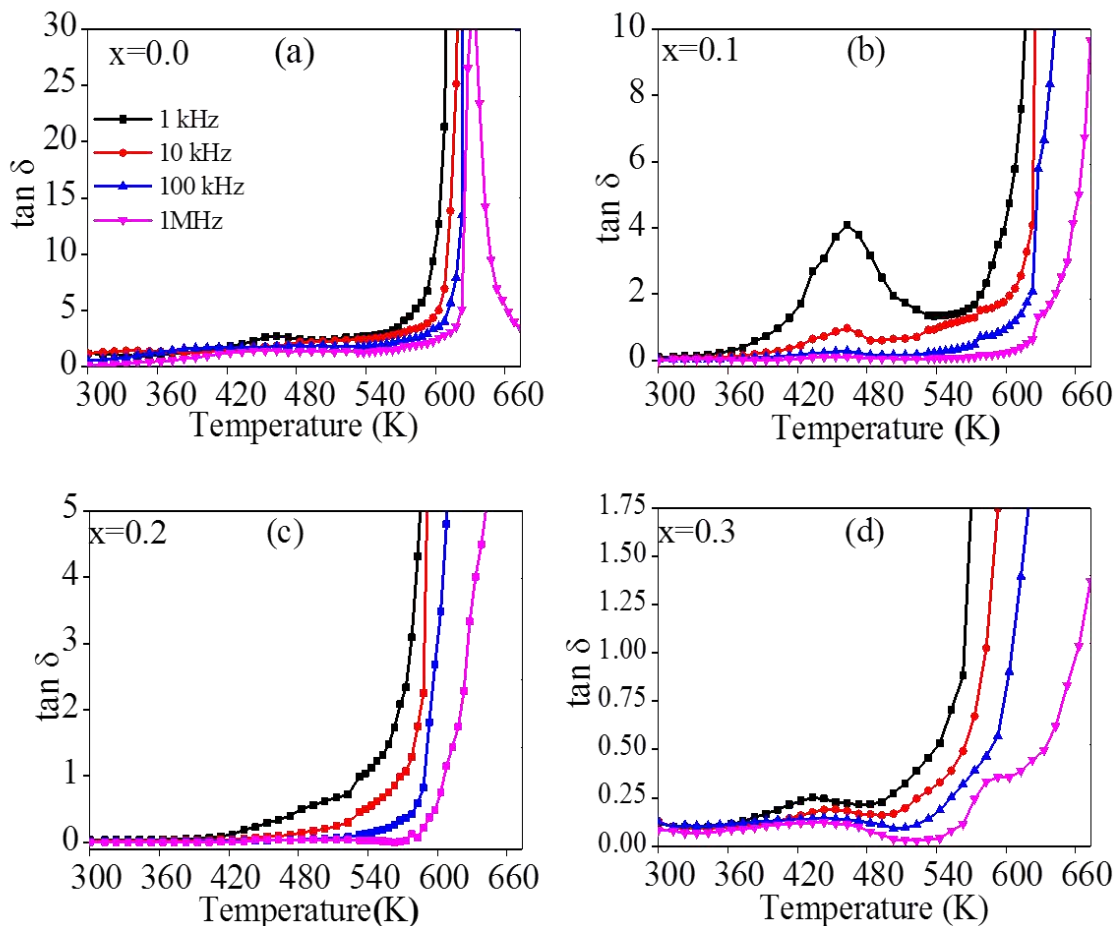


Fig. 7 Temperature dependence of dielectric loss ($\tan \delta$) at different frequencies for $(1-x)\text{BFO} - (x)\text{CTO}$ [$x=0, 0.1, 0.2$ and 0.3]

3.3 Electrical conductivity

Their electrical conductivity reveals the electrical characteristic of the materials. The frequency dependent characteristic is shown in Fig. 8. The plot is divided into two frequency regions: low (1kHz-10kHz) and high (10kHz-1MHz). The low-frequency region corresponds to dc conductivity as it is almost frequency independent. In the high-frequency region, conductivity increases rapidly and this is due to the charge carrier's hopping.

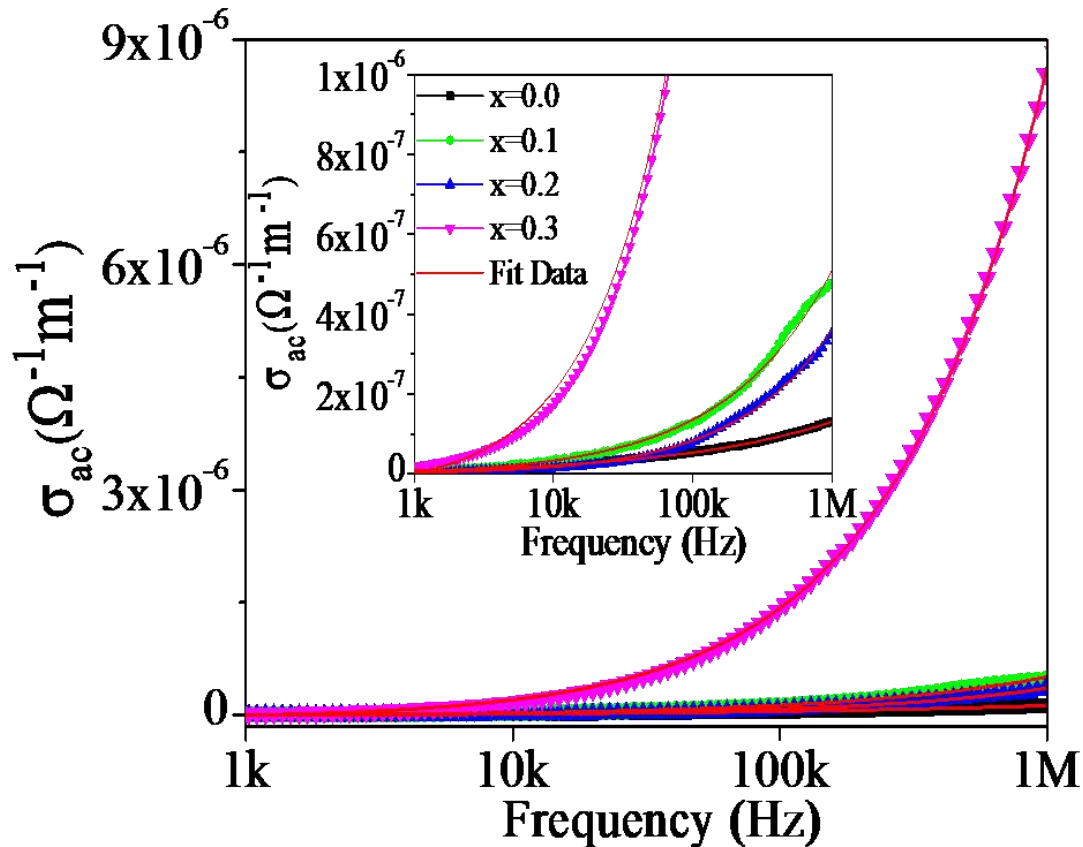


Fig. 8 Variation of ac conductivity with frequency for (1-x)BFO – (x) CTO [x=0, 0.1, 0.2 and 0.3] at room temperature

In general, the frequency dependence of ac conductivity can be analyzed by Jonscher's power law [49], which is given below:

$$\sigma_{ac} = \sigma_{dc} + A\omega^n \quad (1)$$

where, A is the dispersion parameter which represents polarizability, and n is the dimensionless frequency exponent, which represents the interaction between the mobile ions with the surrounded lattice, and its value can be between 0 to 1, i.e. for $n < 1$, a translational motion is a consequence with spontaneous hopping of charge carrier and for $n > 1$, the localized hopping takes place without departing the neighbourhood species [50]. According to this law, the frequency dependence of conductivity arises due to mobile charge carriers' motion by using the relaxation phenomenon [51]. Mobile ions jump from a site to its vacant neighbour sites in a low-

frequency region and hop randomly in the high frequency region. Thus, at the high-frequency region, the samples' conductivity is related to high-frequency diffusion of ions by forwarding and backward hopping of charges [52]. The frequency-dependent conductivity data is well fitted by applying Jonscher's power law, and the parameters obtained have been given in Table 1. It is clear from Table 1 that the value of n is less than 1 for all compositions and increases with increasing CTO. This may be due to a decrease in interaction between charge carrier and lattice surrounding them [49].

The conductivity is also plotted with the inverse of absolute temperature at different frequencies (1kHz, 10kHz, 100kHz, and 1MHz) for all composites are shown in Fig. 9. The plot obeys Arrhenius relation, which is given below:

$$\sigma_{ac} = \sigma_0 \exp\left(\frac{Ea}{kT}\right) \quad (2)$$

where σ_0 is the pre-exponential factor, and it is the material's characteristic, Ea is the activation energy for conduction, k is the Boltzmann's constant, T is the absolute temperature. From the plots, it is observed that the conductivity increases with increasing temperature showing negative temperature coefficient of resistance (NTCR) behaviour. The plots are divided into three temperature regions, namely low-temperature region (313-453)K, intermediate temperature region [(453-553)K and (553-623)K] and high-temperature region (623-713)K. The activation energy can be calculated from the linear fitted slope of different regions and also by equation (2).

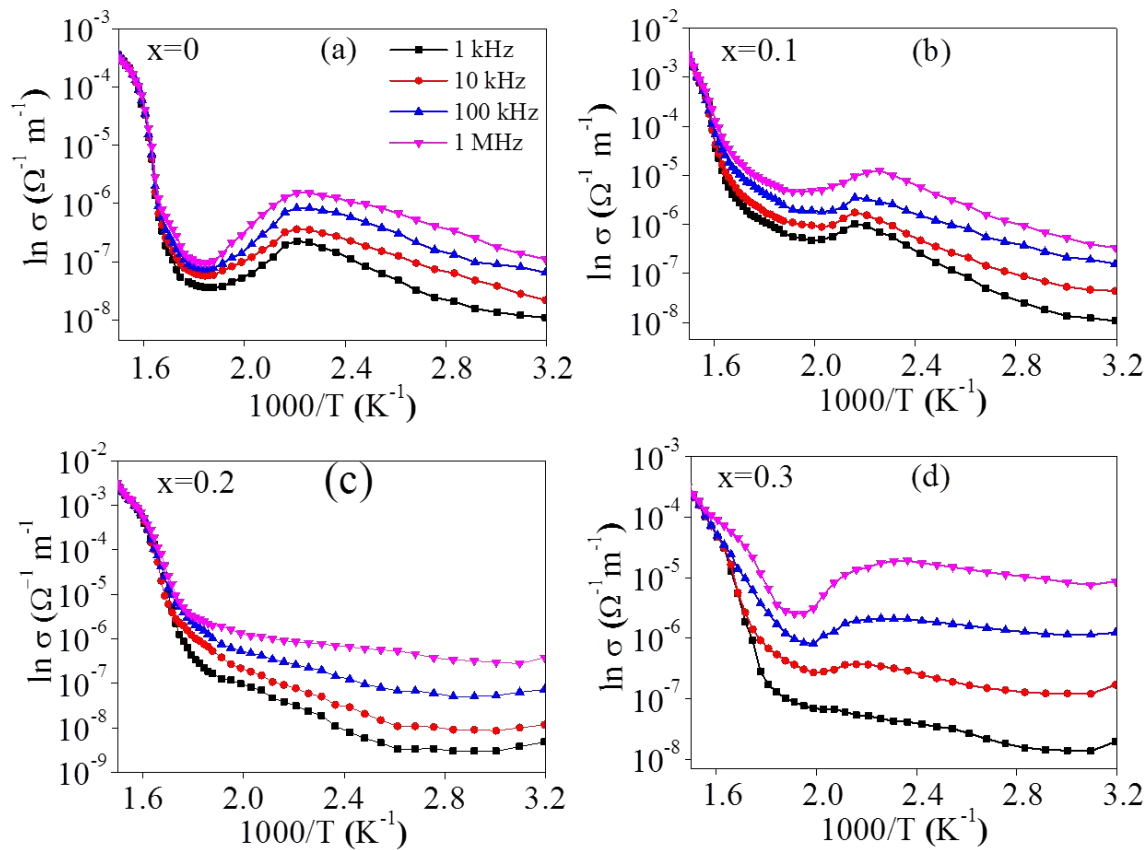


Fig. 9 Variation of ac conductivity with inverse of temperature for (1-x)BFO – (x)CTO [x=0, 0.1, 0.2 and 0.3]

The calculated activation energies are tabulated in Table 2. As temperature increases, dispersion becomes narrow, and all the curves of different frequencies amalgamate into a single curve at high temperatures due to the recombination of released space charges. Each frequency plot with different slopes suggests different types of conduction processes with different activation energies. From Fig. 8, it is clear that conductivity varies slowly in the low-temperature region, which reveals the hopping of charge carriers [53-57]. In the low-temperature region, the activation energy is low, which is due to the effect of electronic contribution to conductivity in which hopping of charge carriers may be due to the localized states in a disordered manner [58]. In the high-frequency region, conductivity increases rapidly due to the bismuth and oxygen vacancies arising due to the bismuth and oxygen ions evaporation and substitution of Ti^{4+} in the samples. Hence, charge neutrality will maintain. These charge compensations are followed by Kroger – Vink equation as shown below [59]:

$$O_0^x = \frac{1}{2}O_2 + V_0^{**} + 2e^{\bullet} \quad (3)$$

During the sintering process, such types of defects were created and leave behind free-electron making material n-type. It is also observed that the conductivity in low temperature is of the order of 10^{-8} , which increases up to 10^{-2} in high temperature. This increase in conductivity is due to the ionization of defects and charge carriers created.

3.4 Leakage current

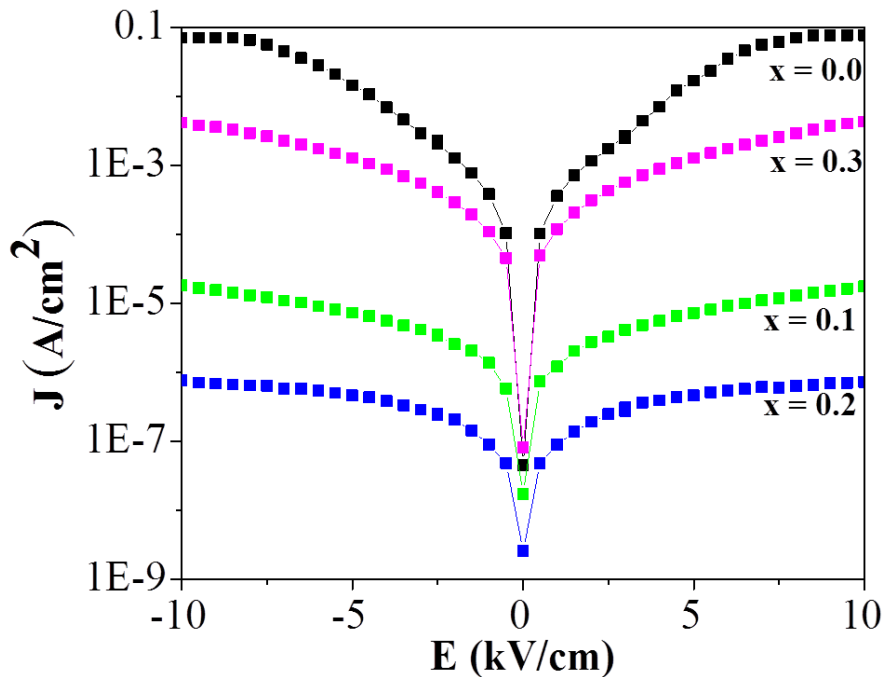


Fig. 10 Leakage current densities (J) as a function of electric field (E) for $(1-x)$ BFO – (x) CTO ($x=0, 0.1, 0.2$ and 0.3)

Fig. 10 shows the leakage current density (J) with respect to electric field (E) of the $(1-x)$ BFO – (x) CTO with $x=0, 0.1, 0.2$ and 0.3 at room temperature. The leakage current density increases progressively as the field increases. The measured values of J for BFO and composites at an electric field of 10kV/cm are 3.58×10^{-5} ,

8.89×10^{-7} , 4.18×10^{-8} and 4.37×10^{-6} A/cm², respectively. Hence, it is clear that, for $x=0.2$ composition, the leakage current reduces drastically compared to BFO and increases again for 0.3. This may be due to the phase change i.e. for $x=0.1$, and $x=0.2$, the monoclinic phase should be maintained, and this contributes to decrement in leakage current, and for $x=0.3$, increment in leakage current is due to the structure change from monoclinic to a non-polar orthorhombic structure.

The decrease in leakage current is due to the valence fluctuation of Fe^{2+}/Fe^{3+} and oxygen vacancies (V_O). This can be endorsed due to the volatilization of Bi ion in the lattice, which induces the removal of oxygen vacancies. Also, the bond dissociation energy of Ca-O is larger than the Bi-O bond; hence Ca-O bond cannot easily be broken by application of field as compared to Bi-O bond [60]. Furthermore, the substitution of Ti^{4+} ions results in the formation of Ti_{Fe}^{2+} for divalent Fe ion and Ti_{Fe}^{3+} for trivalent Fe ion, which eliminates the oxygen vacancies and maintains charge balance [61]. Therefore, the substitution of divalent cations on A-site and tetravalent Ti on B-site efficiently restrains the oxygen vacancies and reduces the current leakage density. The composition of CTO is also an important factor in reducing the leakage current.

3.5 Magnetic field study

Fig. 11 shows the M-H loop for $(1-x)BFO - (x)CTO$ with $x=0, 0.1, 0.2$ and 0.3 compositions measured by vibrating sample magnetometer (VSM) at an applied field of 1T at room temperature (300K). Enhancement of magnetization by increasing CTO concentration was observed. The remnant magnetization (H_r) and coercive (H_c) fields for all the samples are presented in Table 3, which clearly indicates that the remnant magnetization and coercive field increase with the CTO concentration. For all the samples, a non-zero remnant magnetization and non-saturated MH loop were observed, and it reveals the presence of antiferromagnetic property with weak ferromagnetism [62].

According to Yuan and Or et al. [63], $BiFeO_3$ shows a linear, very weak magnetization on applying magnetic field due to suppression of the space-modulated spin structure. By introducing $CaTiO_3$ in $BiFeO_3$ to form the solid solution, the spin accent unusual to $BiFeO_3$ is dormant [64]. Through the introduction of $CaTiO_3$, the amount of magnetic Fe^{3+} decreased, and the antiferromagnetic structure of $BiFeO_3$ may be destroyed. Hence, very small net magnetization was observed in the samples. Alternatively, the cycloidal structure's stability in an external magnetic field can be adequately influenced by substituting elements of different sizes. The data suggest that the effective way to reduce the critical field is to replace Bi^{2+} ions with smaller ionic radius ions when compared with an approach of using the dopants $r > r_{Bi^{3+}}$.

For the composite solid solutions with high Ca/Ti ion concentrations, the magnetic dilution effect becomes more prominent, and continuous magnetization diminution takes place observed for $x=0.3$ in Fig. 11. The compounds' magnetization is considered by a continuous transformation of remnant magnetic moment across the phase transition from monoclinic to orthorhombic phase. The bond overlapping of oxygen p orbital and iron d orbital is associated with continuous changes of the magnetization across the phase boundary, and the structure alters the relative positions of consequent ions $Fe(3d) - O(2p)$ orbital hybridization as well as the remanent magnetization of the compounds [65 -67] in both structural phases. Hence, it is clear that the CTO addition in composites only suppresses the cycloidal structure of BFO. We also observe that the magnetization

of $(1-x)\text{BFO} - (x)\text{CTO}$ gradually reduces after $x=0.3$ due to the diamagnetic nature of CTO reveals that the dopant concentration (CTO) effects the magnetic properties.

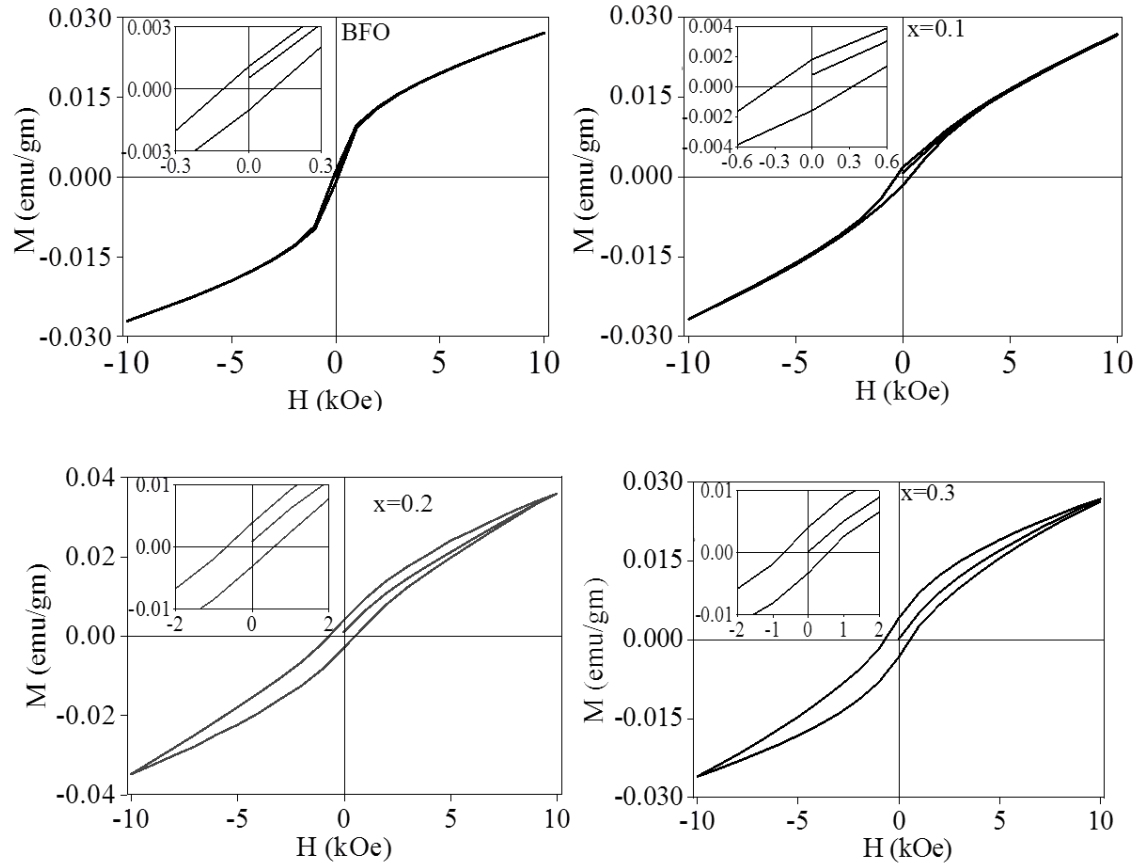


Fig. 11 Hysteresis loop for $(1-x)\text{BFO} - x\text{CTO}$ ($x=0, 0.1, 0.2$ and 0.3)

3.6 Magneto-dielectric properties

Fig. 12 shows the magneto-dielectric (MD) effect in $(1-x)\text{BFO} - (x)\text{CTO}$ [$x=0, 0.1, 0.2$ and 0.3] compositions. For this, the dielectric permittivity of BFO-CTO compositions was measured at different magnetic fields (0.25, 0.50, 0.75 and 1.0 Tesla) in the frequency range from 100Hz to 1MHz at room temperature and presented in Fig.12. It can be seen from Fig. 12 that for pure BFO, the value of dielectric permittivity decreases with the applied magnetic field in the frequency range of ~ 100 Hz to ~ 905 Hz, and after that, the value increases in the frequency range from ~ 905 Hz to 1MHz. Thus it is indicated that BFO exhibit negative magneto-electric coupling below ~ 905 Hz and positive magneto-electric coupling above 905 Hz. A similar result is observed for the $0.9\text{BFO} - 0.1\text{CTO}$

The other two compositions ($0.8\text{BFO} - 0.2\text{CTO}$ and $0.7\text{BFO} - 0.3\text{CTO}$) show only negative magneto-dielectric coupling because the dielectric permittivity decreases with the applied magnetic field. J. Pal et al. [68] also observed the negative and positive magneto-dielectric coupling in $\text{BiFeO}_3\text{-BaSrTiO}_3$ system. Hence, it is observed that the magneto-dielectric behaviour may be due to coupling between ferroelectric domains and

magnetic domains [67,68]. Due to this coupling, the ferroelectric/ferrite composite gets strain on the magnetic field application, and this strain induces stress and produces an electric field on the ferroelectric domains [69].

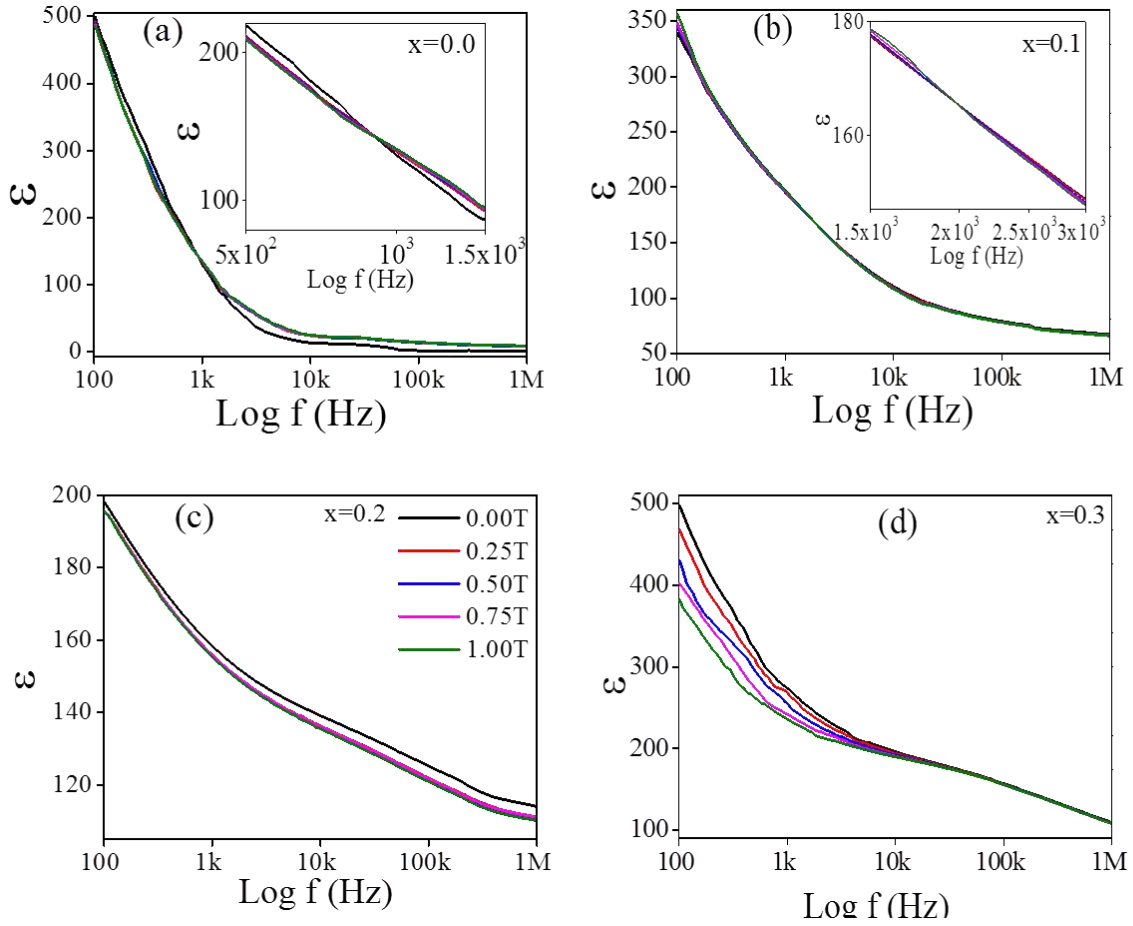


Fig. 12 Frequency response of dielectric permittivity at room temperature at different magnetic field (0, 0.25, 0.50, 0.75 and 1 Tesla) for (1-x) BFO – (x) CTO [x=0, 0.1, 0.2 and 0.3]

Fig. 13 shows the magneto-dielectric coupling of pure BFO [inset] and composite co-doped samples at 100Hz. The magneto-dielectric data gives the information about the percentage change in dielectric permittivity in the presence of a magnetic field [70, 71] and is defined as:

$$MD (\%) = \frac{(\varepsilon_H - \varepsilon_0)}{\varepsilon_0} \times 100$$

where, ε_H and ε_0 denote the dielectric permittivity at the applied magnetic field and zero fields, respectively. The MD values of all the compositions are tabulated in Table 4 at 1kHz at different fields. It is clear from Table 4 that the MD values increase with increasing field. The observed values of MD at 100 Hz (from Fig. 12) and an applied field of 1T for $(1-x)\text{BFO} - (x)\text{CTO}$ with $x=0, 0.1, 0.2$ and 0.3 compositions are -2.62, 4.99, -1.26, and -23.19 respectively.

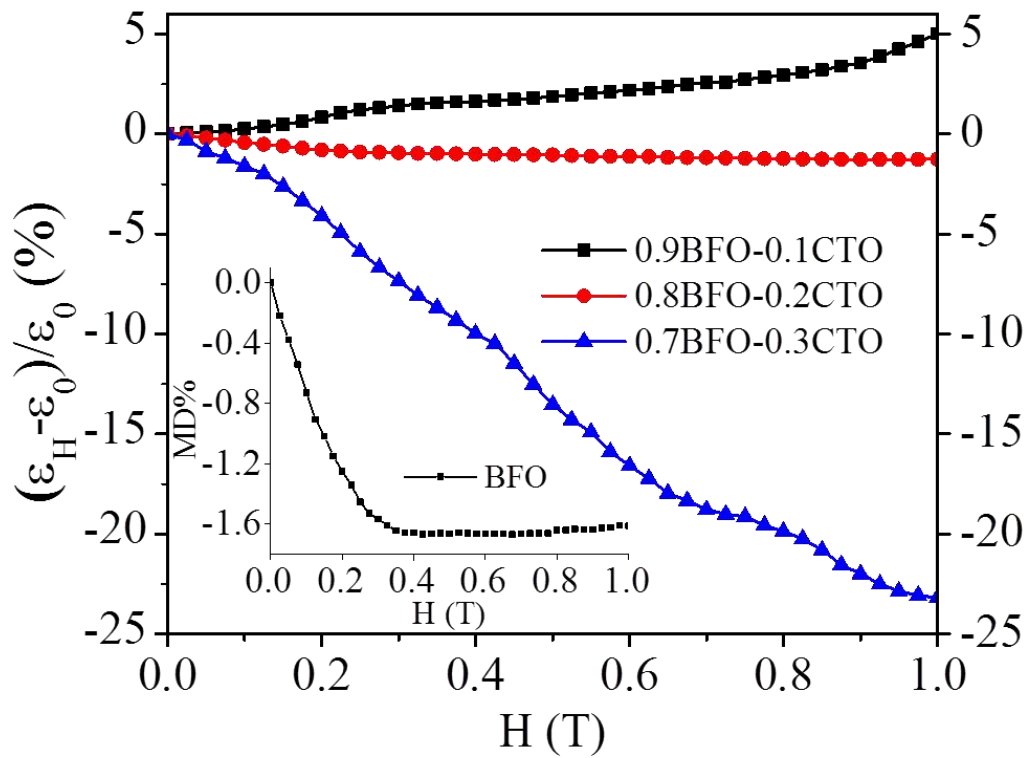


Fig. 13 MD% versus magnetic field for $(1-x)\text{BFO} - (x)\text{CTO}$ [$x=0, 0.1, 0.2$ and 0.3] (the inset Fig. shows MD plot for BFO)

The anomalous change in MD of $(1-x)\text{BFO} - (x)\text{CTO}$ compositions may be due to a change in magnetic properties and breakage of the spin cycloid structures with an increase in CTO concentration from $x=0.1$ to 0.3 . It can be seen that the $0.7\text{BFO} - 0.3\text{CTO}$ shows ~20% enhanced magneto-dielectric value than that of pure BFO due to change in lattice parameter arises due to different size of dopant ions Ca^{2+} and Ti^{4+} in the Bi^{3+} and Fe^{3+} site of BiFeO_3 . This change in lattice parameter leads to structural strain, which gets improved with magnetic field application in the doped samples. The magnetic field produces piezoelectric stress in $(1-x)\text{BFO} - (x)\text{CTO}$ samples, which results in electric field generation in the ferroelectric domains, and in results, these samples show strong magneto-dielectric coupling at room temperature[67,68].

4 Conclusions

A single-phase $(1-x)\text{BiFeO}_3-x\text{CaTiO}_3[(1-x)\text{BFO} - (x)\text{CTO}]$ ($x=0.0, 0.1, 0.2$ and 0.3) composite were effectively synthesized by using the sol-gel method. The structural investigation confirms the rhombohedral structure with space group R_3c for $x=0$ and monoclinic phase with space group Cc for ($x= 0.1, 0.2$) and orthorhombic phase with space group $Pbnm$ for $x=0.3$. The FESEM reveals that the microstructure consists of randomly oriented, homogenous, and non-uniform grains. Also, the size of grains decreases upto $x= 0.2$ and

after that, it increases. This may be due to structural change from monoclinic to orthorhombic. The frequency (from 1kHz to 1MHz) and temperature dependence of dielectric permittivity and tangent loss for $(1-x)\text{BFO} - x\text{CTO}$ for $x=0.0, 0.1, 0.2$ and 0.3 composite were investigated. The behaviour of dielectric permittivity is explained using dielectric relaxation and the Maxwell-Wagner polarization model. An anomalous change in dielectric permittivity and tangent loss were observed for all compositions at high temperatures may be due to the effect of structural phase transition. It is also observed that with increasing CTO concentration in BFO, the magnetic phase transition temperature reduces. The frequency-dependent ac conductivity obeys Johncher's power law. The value of ac conductivity increases by increasing CTO concentration, which implies that the addition of CTO in BFO helps increase the number of charge carriers, contributing to an increase in the AC conductivity. The conductivity increases are due to the ionization of defects and the charge carriers created in the samples. A drastic reduction in the leakage current is observed for $0.8\text{BFO}-0.2\text{CTO}$ compared to other compositions. The M-H loop for $[(1-x)\text{BFO} - (x) \text{CTO}]$ ($x=0.0, 0.1, 0.2$ and 0.3) samples at room temperature shows the presence of weak ferromagnetic property, which increases effectively with doping concentration. Pure BFO and $0.9\text{BFO}-0.1\text{CTO}$ show positive and negative magneto-dielectric coupling, whereas $0.8\text{BFO}-0.2 \text{CTO}$ and $0.7\text{BFO}-0.3\text{CTO}$ shows negative magneto dielectric coupling. The high dielectric permittivity, low tangent loss, good conductivity, high magnetization, very low leakage current, and strong magneto-dielectric coupling at room temperature make $(1-x)\text{BFO} - (x) \text{CTO}$ [$x=0.0, 0.1, 0.2$ and 0.3] compositions an interesting material for the possible next-generation spintronics and multifunctional device applications.

Acknowledgment

We wish DST, Government of India for financial support to the Centre of Materials Sciences, under FIST Programme. B Khan thankfully acknowledges the University Grant Commission (UGC) of India for providing UGC research fellowship. The author Manoj Singh is grateful to UGC India for financial support under the major research project (grant No. 39-869/2010).

References:

- [1] Ma J, Hu J, Li Z, Nan C-W, *Adv Mater* 23, 1062–1087(2011)
- [2] Eerenstein W, Mathur ND, Scott JF, *Nature* 442, 759–765(2006)
- [3] I. Sosnowska, T.P. Neumaier, E. Steichele, *J. Phys. C. Solid State Phys.* 15,4835–4846(1982)
- [4] S.M. Selbach, T. Tybell, M.A. Einarsrud, *Adv. Mater.* 20,3692–3606(2008)
- [5] F. Kubel, H. Schmid, *Acta Crystallogr. B* 46,698–702(1990)
- [6] C. Ederer, N.A. Spaldin, *Phys. Rev. B* 71 060401(2005)
- [7] Meera Rawat, K.L. Yadav, *J. Alloys Comp.* 597,188-1999(2014)
- [8] S. Narendra Babu, Jen-Hwa Hsu, Y.S. Chen, J.G. Lin, *J. Appl. Phys.* 109,07D904(2011)
- [9] D.R. Patil, B.K. Chougule, *J. Alloys Comp.* 470, 531–535(2009)
- [10] N.M. Burange, S.S. Chougule, D.R. Patil, R.S. Devan, Y.D. Kolekar, B.K. Chougule, *J. Alloys Comp.* 479,569–573(2009)
- [11] J. Van Suchtelen, *Philips Res. Rep.* 27,28–37(1972)
- [12] S.H. Jo, S.G. Lee, Y.H. Lee, *Nanoscale Res. Lett.* 7,54(2012)
- [13] G. Catalan, J.F. Scott, *Adv. Mater* 21,2463(2009)

- [14] J. Wang, J. Neaton, H. Zheng, V. Nagarajan, S. Ogale, B. Liu, D. Viehland, V. Vaithyanathan, D. Schlom, U. Waghmare, *Science* 299,1719(2003)
- [15] T. Zhao, A. Scholl, F. Zavaliche, K. Lee, M. Barry, A. Doran, M. Cruz, Y. Chu, C. Ederer, N. Spaldin, *Nature* 5,823(2006)
- [16] J.G. Wu, D.Q. Xiao, J.G. Zhu, *Chin. Sci. Bull.* 59, 5205(2014)
- [17] A. Hussain, X. Xu, G. Yuan, Y. Wang, Y. Yang, J. Yin, J. Liu, Z. Liu, *Chi. Sci. Bull.* 59,5161(2014)
- [18] T. Rojac, A. Bencan, B. Malic, G. Tutuncu, J.L. Jones, J.E. Daniels, D. Damjanovic, D.J. Green, *J. Am. Ceram. Soc.* 97,1993(2014)
- [19] Qiaoji Zheng, Lingling Luo, Kwok Ho Lam, Dunmin Lin, *J. App. Phys.* 116, 184101 (2014)
- [20] G.L. Yuan, S.W. Or, J.M. Liu, Z.G. Liu, *Appl. Phys. Lett.* 89,052905(2006)
- [21] V.R. Palkar, D.C. Malik, S. Bhattacharya, *Phys. Rev. B* 69,212102-212103(2004)
- [22] V.V. Lemanov, A.V. Sotnikov, E. Psminova, M. Weihnacht, R. Kunze, *Solid State Commun.* 110,611(1999)
- [23] I.S. Kim, M. Itoh, T. Nakamura, *J. Solid States Chem.* 101,77(1992)
- [24] Qing Qing Wang, Hong Jain Zhao and Xiang Ming Chen, *J. App. Phys.* 111, 126101(2012)
- [25] Shalini Kumari, N. Ortega, A. Kumar, J.W. Hubbard, Ram S. Katiyar, *J. App. Phys.* 117,114102(2015)
- [26] R. Palai, R.S. Katiyar, H. Schmid, P. Tissot, S.J. Clark, J. Robertson, S.A.T. Redfern, G. Catalan, J.F. Scott, *Phys. Rev. B* 77,014110-014111(2008)
- [27] Vijay Kumar, Akhilesh Kumar Singh, Satyendra Singh, *J. App. Phys.* 112, 204101(2017)
- [28] I. Troyanchuk, D. Karpinsky, M. Bushinskii, O. Prokhnenko, M. Kopcevicz, R. Szymczak, J. Pietosa, *J. Exp. Theor. Phys.* 107,83-89(2008)
- [29] K. Sen, K. Singh, A. Gautam, and M. Singh, *Ceram. Int.* 38,243(2012)
- [30] R.K. Dwivedi, D.Kumar, O.Parkash, *J. Mater. Sci.* 36, 3657-3665(2001)
- [31] Hang Q, Xing Z, Zhu X, Yu M Y, Song M, Zhu J and Liu Z, *Int.* 38S S411 (2012)
- [32] J.C. Maxwell, *Electricity and Magnetism*, Oxford University Press(London, 1973)
- [33] K.W. Wagner, *Ann. Phys.* 40,818(1993)
- [34] E.V. Gopalan, K.A. Malini, S. Saravanan, D. Sakthi Kumar, Y. Yoshida, M.R. Anantharaman, *J. Phys. D Appl. Phys.* 41,185005(2008)
- [35] C.G. Koops, *Phys. Rev.* 83,121–124(1951)
- [36] Gulab Singh, H P Bhasker, R P Yadav, Aditya Kumar, Bushra Khan, Ashok Kumar and Manoj K Singh, *Phys. Scr.* 94,065802(2019)
- [37] Durgadimi S U, Chougale S S, Chougale B K, Bhosle C H and Bellad S S, *Mater. Chem. Phys.* 131, 199(2011)
- [38] V.A. Isupov, *Ferroelectrics* 90,113-118(1989)
- [39] V. Goian, S. Kamba, M. Savinov, D. Nuzhnyy, F. Borodavka, P. Vaněk, *J. App. Phys.* 112,074112(2012)
- [40] E. Palaimiene, J. Macutkevic, D. Karpinsky, A. Kholkin, and J. Banys, *App. Phys. Lett.* 106,012906(2015)

- [41] V. Palkar, D. C. Kundaliya, S. Malik, and S. Bhattacharya, *Physical Review B* 69,212102(2004)
- [42] W. Eerenstein, N. D. Mathur, and J. F. Scott, *Nature* 442,759(2006)
- [43] R. Ramesh and N. A. Spaldin, *Nature Materials*6,21(2007)
- [44] F. Mizouri, I. Kallel, N. Abdelmoula, D. Mezzane, H. Khemakhem, *J. Alloys and Compounds* 731,458-464(2018)
- [45] W.M. Zhu, Z.G. Ye, *Ceram. Int.* 30,1435-1442(2004)
- [46] G.A. Smolenskii, *J. Phys. Soc. Jpn.* 88,26(1970)
- [47] B. N. Parida, R. Padhee, D. Suara, A. Mishra and R. N. P. Choudhary, *J. Mat. Sci.: Mater Electron.* 27,9015-9012(2016)
- [48] L.E. Cross, *Ferroelectrics* 76, 241-267(1987)
- [49] R. K. Dwivedi D. Kumar, O. Parkash, *J. Mat. Science* 36,3649-3655 (2001)
- [50] A.K. Jonscher, *Nature* 267,673(1977)
- [51] D.K. Pradhan, B. Behera, P.R. Das, *J. Mater. Sci.: Mater. Electron.* 23,779(2012),
- [52] J.C. Dyre, Th.B. Schroder, *Phys. Stat. Sol. B* 23,5(2002)
- [53] J.M. Le Meins, O. Bohnke, G. Courbion, *Solid State Ionics* 111,67–75(1998)
- [54] Z. Lu, J.P. Bonnet, J. Ravez, Hagen-muller, *Solid State Ion.* 57,235-244(1992)
- [55] B.H. Venkataraman, K.B.R. Verma, *Solid State Ion.* 167,197-202(2004)
- [56] P. Banarji Behera, P. Nayak, R.N.P. Choudhary, *Mater. Chem. Phys.* 106,193(2007)
- [57] C. Verdier, F.D. Morrison, D.C. Lupascu, J.F. Scott, *J. Appl. Phys.* 97,024107(2005)
- [58] A.R. James, S. Priya, K. Uchino, K. Srinivas, *J. Appl. Phys.* 90,3504-3508 (2001)
- [59] Dhiren K. Pradhan, Pankaj Mishra, Venkata S. Puli, Satyaprakash Sahoo, Dilip K. Pradhan and Ram S. Katyar, *J. Appl. Phys.* 115, 243904(2014)
- [60] Subhash Sharma, Vikash Singh and R. K. Dwivedi, *J. Alloys and Compounds* 682, 723-729(2016)
- [61] Dean JA, Lange's handbook of chemistry, 15thedn. (McGraw-Hill, New York, 1999)
- [62] Wang Y, Nan C-W, *App. Phys. Lett.* 89, 052903(2006)
- [63] Vijay Kumar, Satyendra Singh, *J. Alloy. Comp.* 732, 350-357(2018)
- [64] G. L. Yuan, S. W. Or, *J. Appl. Phys.* 100, 024109 (2006)
- [65] Manoj K. Singh, W. Prellier, M.P. Singh, Ram S. Katiyar and J.F.Scott, *Phys Rev B*77, 144403(2008)
- [66] K. Prashanthi, B. A. Chalke, K. C. Barick, A. Das, I. Dhiman, and V. R.Palkar, *Solid State Commun.* 149,188 (2009)
- [67] S. Ryu, J.-Y. Kim, Y.-H. Shin, B.-G. Park, J. Y. Son, and H. M. Jang, *Chem. Mater.* 21, 5050 (2009)
- [68] Jaswinder Pal, Sunil Kumar, Lakhwant Singh, Mandeep Singh, *J. Magnetism Magnetic Materials* 441, 339–347(2017)
- [69] V.R. Palkar, D.C. Kundaliya, S.K. Malik, *Phys. Rev. B* 69, 212102-212104(2004)
- [70] N. Adhlakha, K.L. Yadav, *Smart Mater. Struct.* 21, 115021 (2012)
- [71] H. Singh, K.L. Yadav, *Mater. Chem. Phys.* 132, 17-21(2012)
- [72] Dhiren K. Pradhan, Shalini Kumari, Venkata S. Puli, Proloy T. Das, Dillip K. Pradhan, Ashok Kumar, J. F. Scott and Ram S. Katiyar, *Phys. Chem.*19,210 (2017)

Tables:

Table 1: The non-linear fitting parameters of frequency dependent ac conductivity of (1-x)BFO – (x)CTO [0≤x≤0.3]

Samples	A	n
BFO	3.31 E-10	0.38
0.9BFO-0.1CTO	7.46 E-11	0.56
0.8BFO-0.2CTO	2.02 E-11	0.62
0.7BFO-0.3CTO	4.48 E-11	0.77

Table 2: Activation energy obtained by linear fitting of ac conductivity versus inverse of absolute temperature plot at 1kHz for (1-x)BFO – (x)CTO [0≤x≤0.3]

At frequency 1kHz	Activation energy (eV) of different temperature region			
	Low (313 - 453)K	intermediate (453-553)K (553-623)K	high (623-713)K	
BFO	0.29	0.41	2.74	1.73
0.9BFO-0.1CTO	0.42	0.41	0.88	2.99
0.8BFO-0.2CTO	0.03	0.48	2.51	1.47
0.7BFO-0.3CTO	0.09	0.15	2.61	1.34

Table 3: Magnetic parameters obtained by hysteresis loop for (1-x)BFO – (x)CTO [0≤x≤0.3]

Samples	Remanant Magnetization	Coercive field
	H _r (emu/gm)	H _c (Oe)
BFO	0.0010	106.60
0.9BFO-0.1CTO	0.0018	323.83
0.8BFO-0.2CTO	0.0041	534.16
0.7BFO-0.3CTO	0.0041	537.46

Table 4: Magneto-dielectric values obtained at different field for (1-x)BFO – (x) CTO [$0 \leq x \leq 0.3$] at 1kHz

Samples	MD values at different magnetic field (Tesla)			
	0.25T	0.50T	0.75T	1T
BFO	2.39	3.17	3.45	3.99
0.9BFO-0.1CTO	0.10	0.21	0.57	1.13
0.8BFO-0.2CTO	-1.55	-1.94	-1.48	-1.93
0.7BFO-0.3CTO	-2.22	-7.07	-11.5	-13.9

Figures

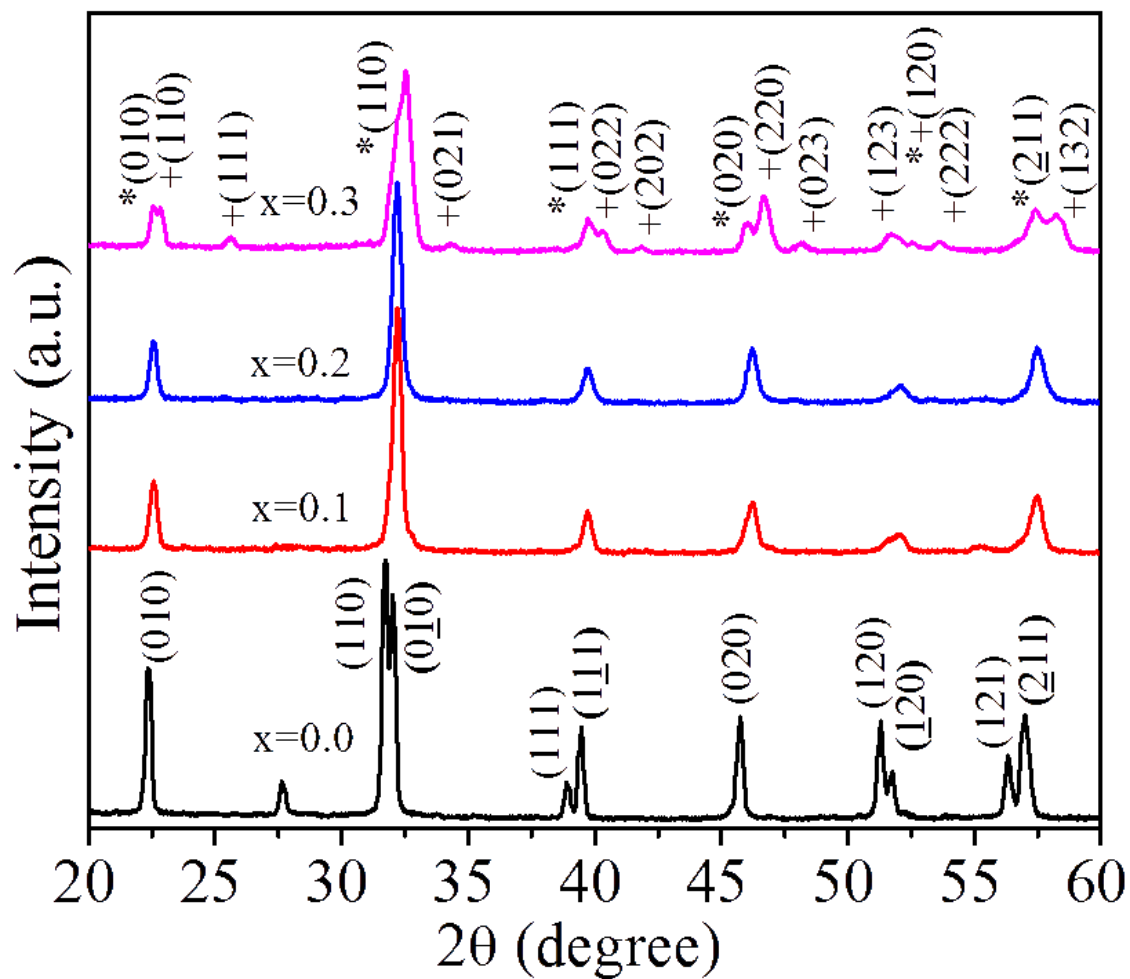


Figure 1

- ray diffraction (XRD) pattern of (1-x) BFO- (x) CTO [x=0, 0.1, 0.2 and 0.3], where (+) denotes ferrite phase and (*) denotes the ferroelectric phase.

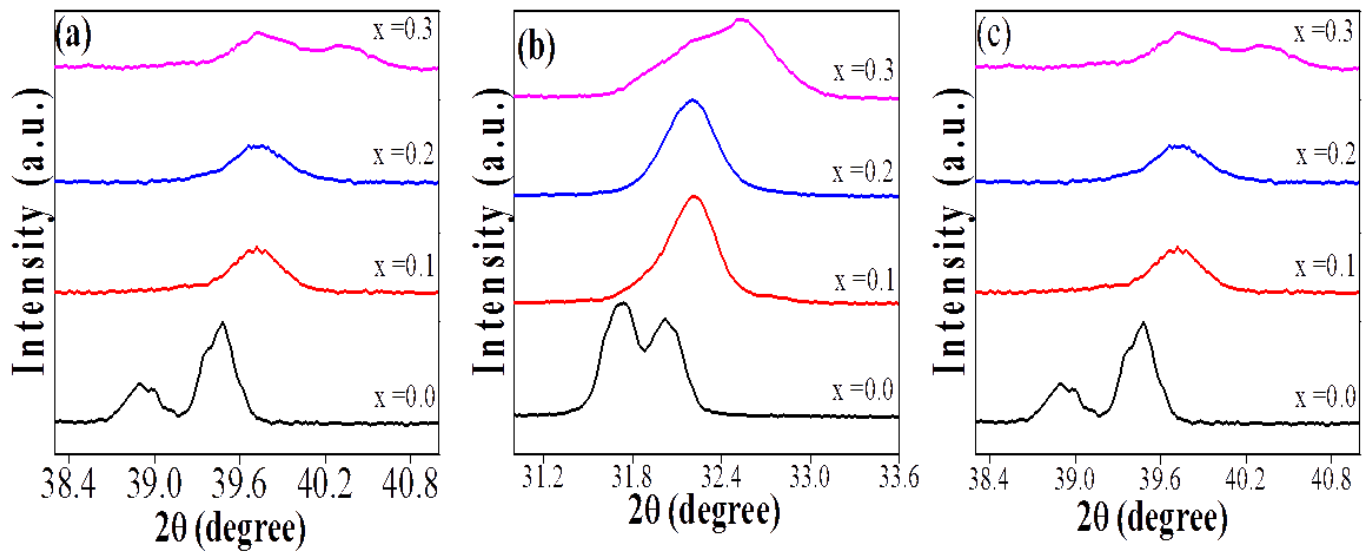


Figure 2

Zoom XRD pattern of (1-x) BFO-(x) CTO [x=0, 0.1, 0.2 and 0.3] to show the peak shifting by enlarge the peaks in 2θ range.

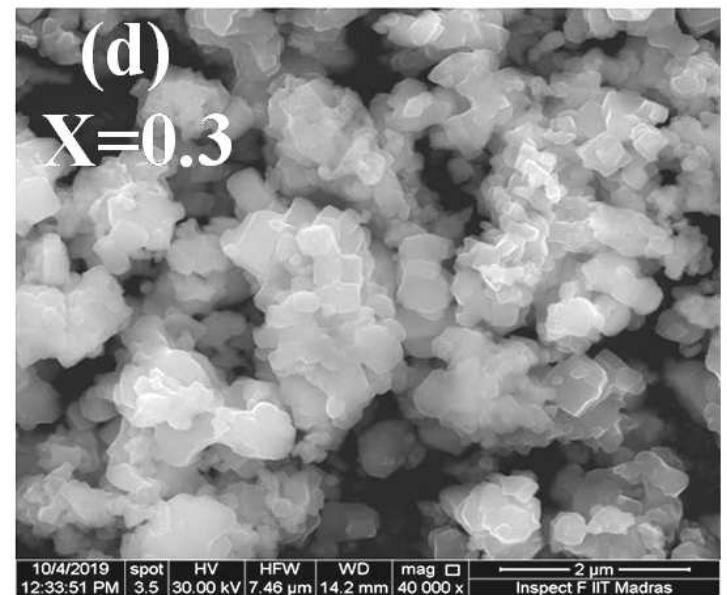
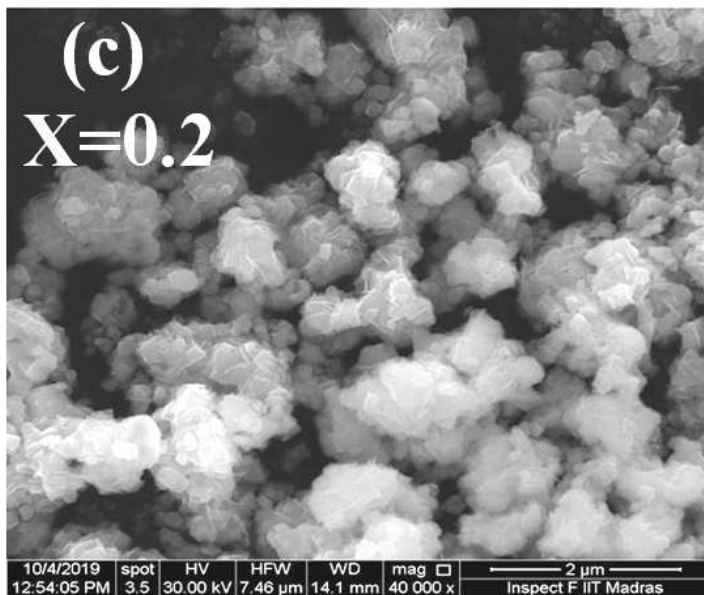
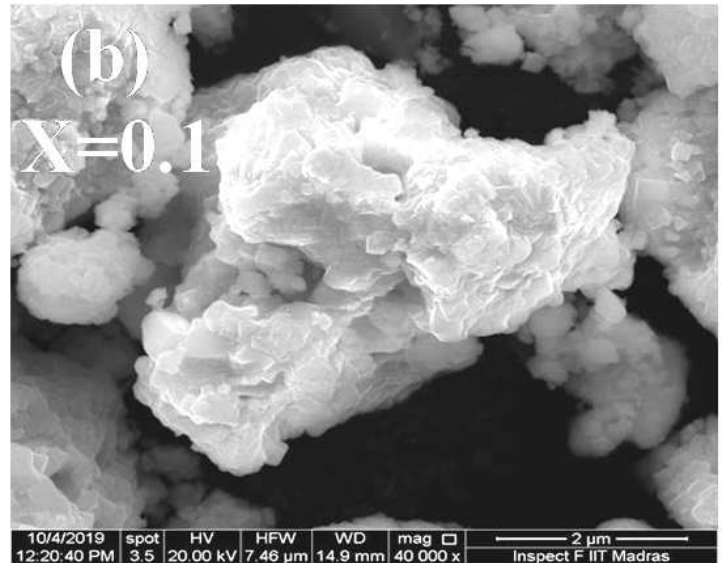
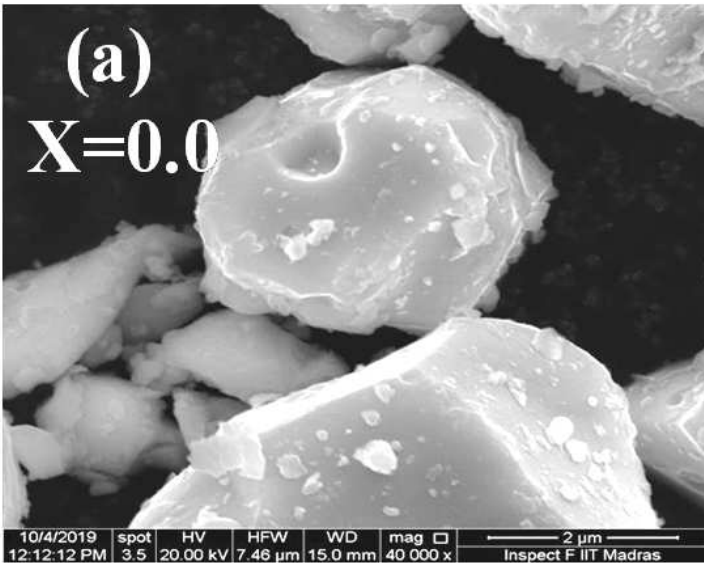


Figure 3

Surface morphology of the $(1-x)\text{BFO} - (x)\text{CTO}$ [$x=0, 0.1, 0.2$ and 0.3]

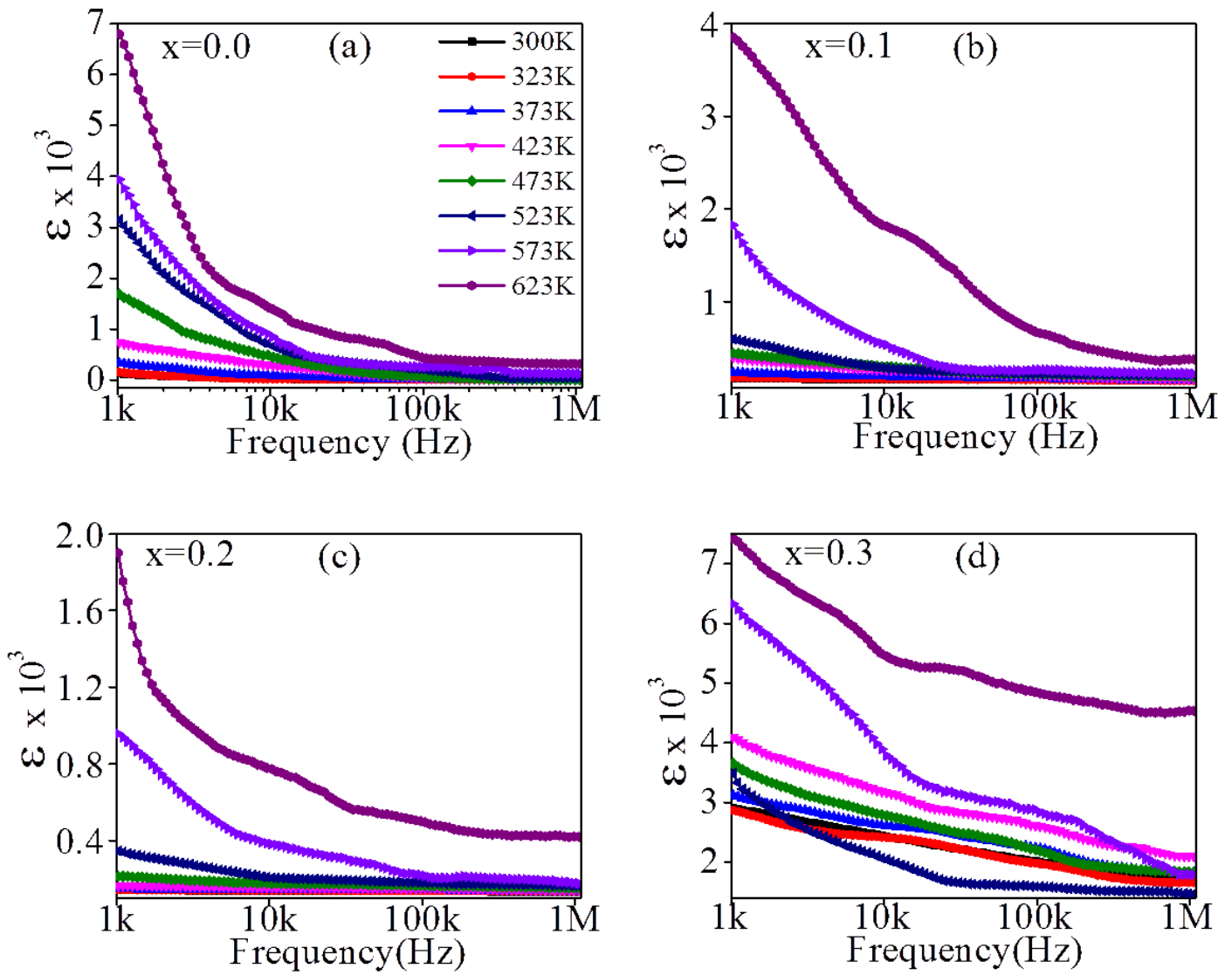


Figure 4

Frequency dependence of dielectric permittivity (ϵ) at selected temperature for $(1-x)\text{BFO} - (x)\text{CTO}$ [$x=0, 0.1, 0.2$ and 0.3]

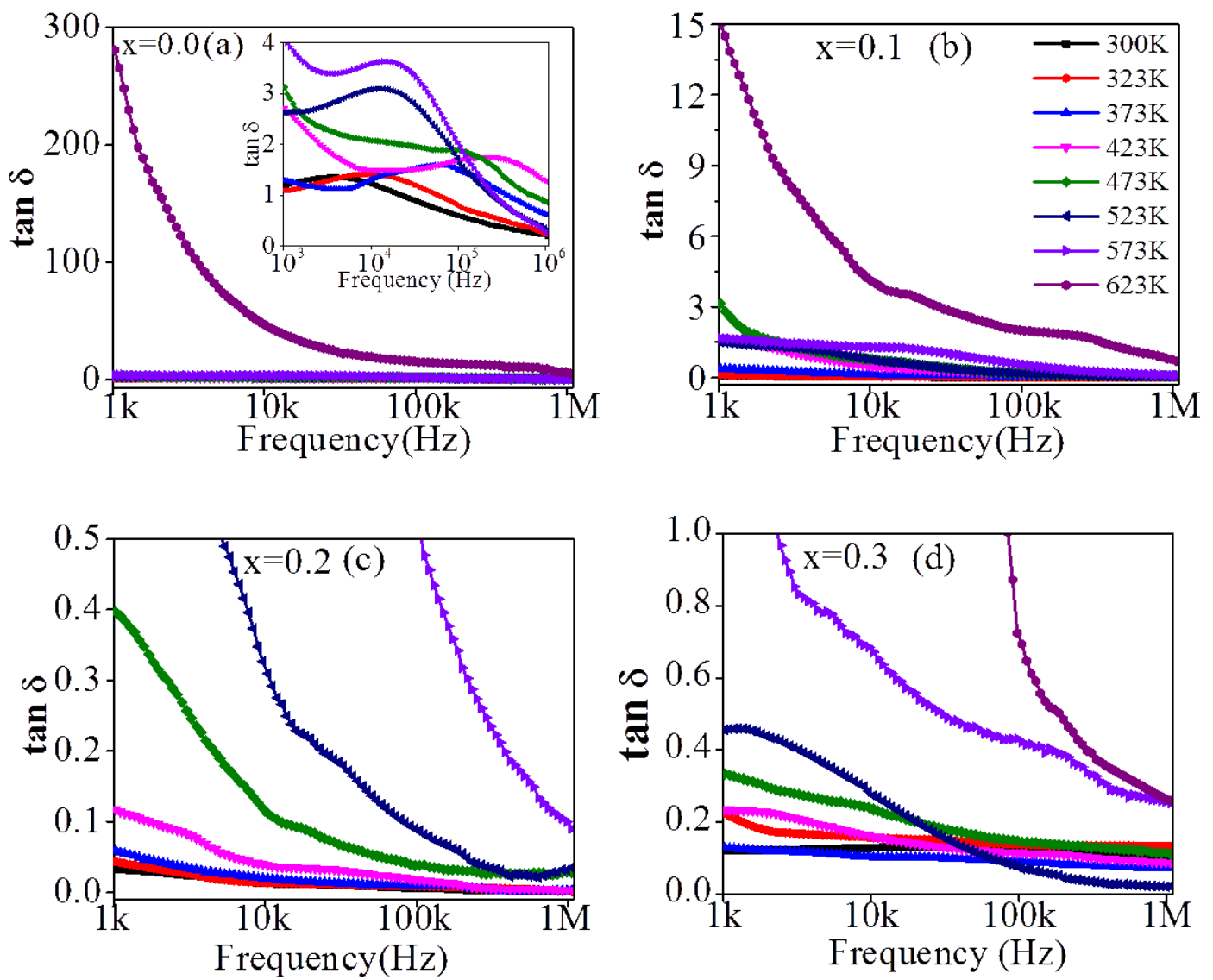


Figure 5

Frequency dependence of tangent loss ($\tan \delta$) at selected temperature for $(1-x)\text{BFO} - (x)\text{CTO}$ [$x=0, 0.1, 0.2$ and 0.3]

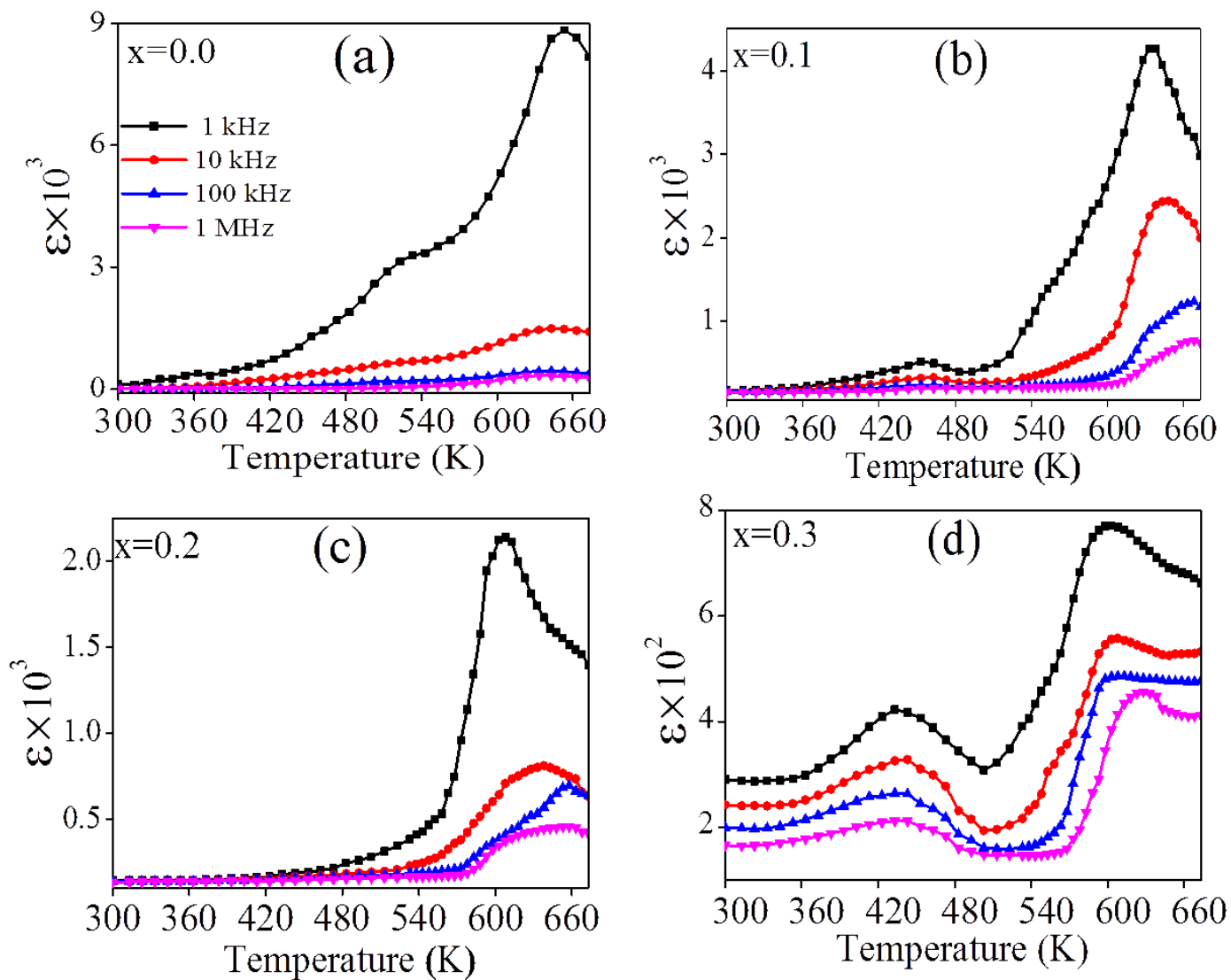


Figure 6

Temperature dependence of dielectric permittivity (ϵ) at different frequencies for $(1-x)\text{BFO} - (x)\text{CTO}$ [$x=0, 0.1, 0.2$ and 0.3]

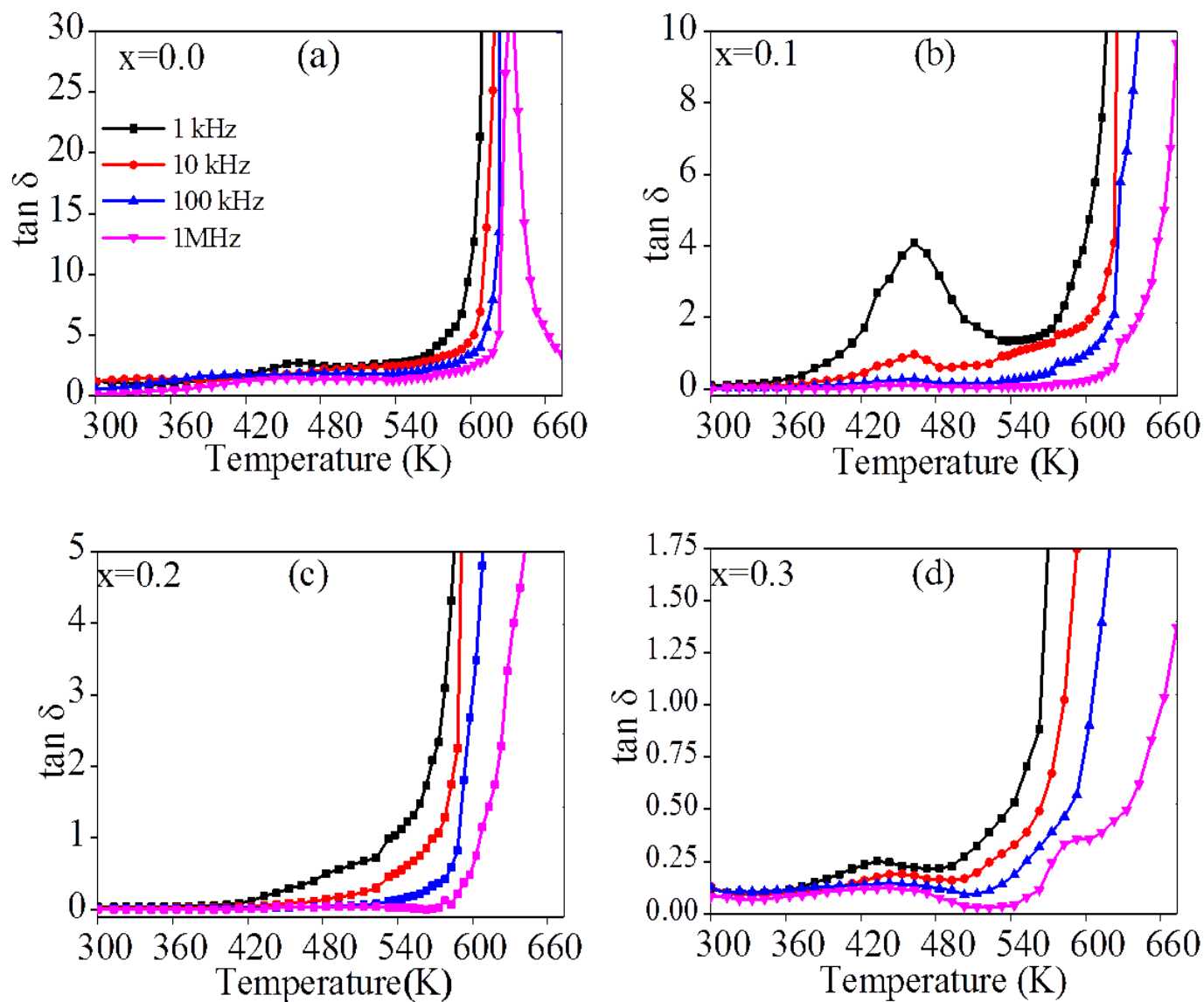


Figure 7

Temperature dependence of dielectric loss ($\tan \delta$) at different frequencies for $(1-x)\text{BFO} - (x)\text{CTO}$ [$x=0, 0.1, 0.2$ and 0.3]

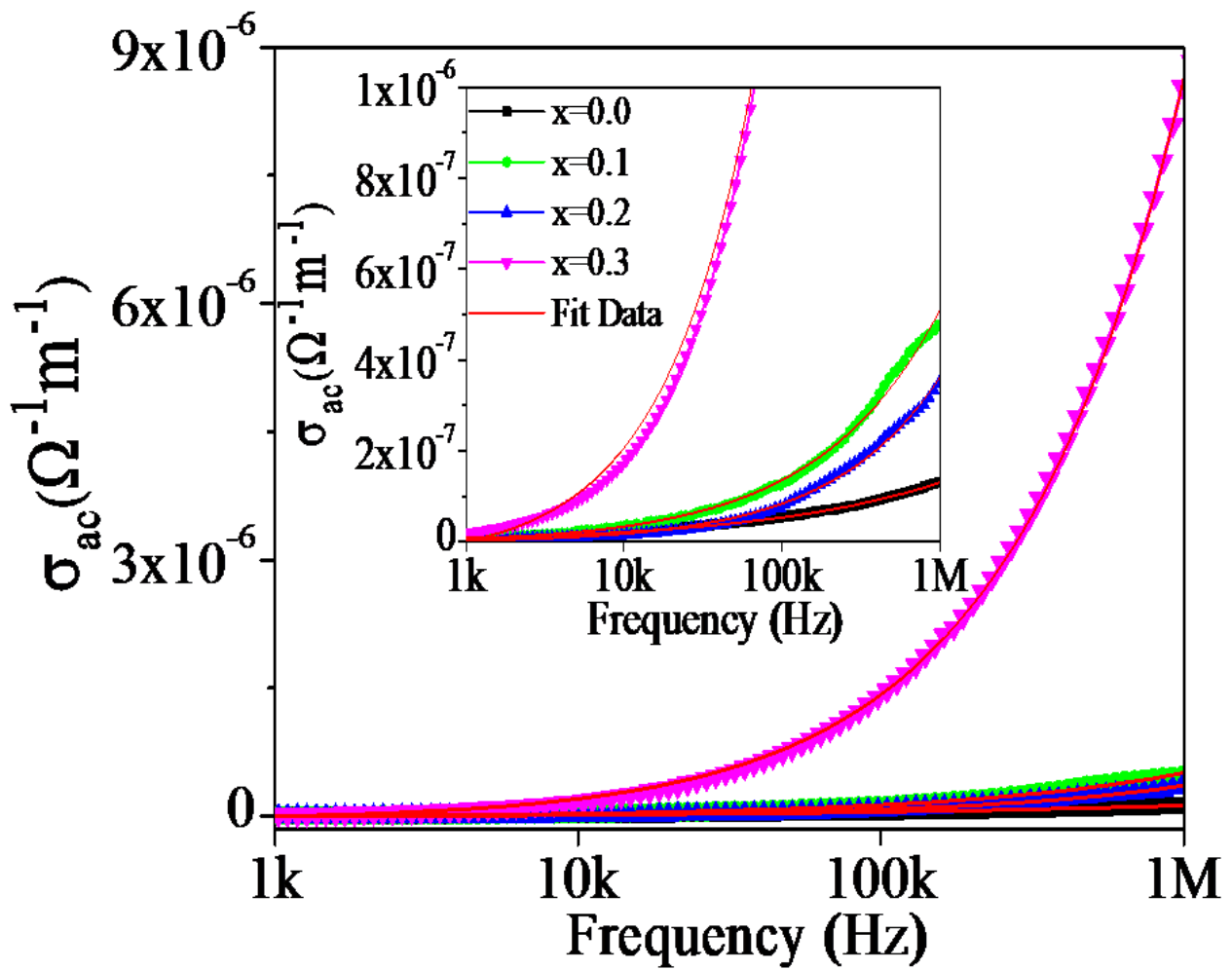


Figure 8

Variation of ac conductivity with frequency for (1-x)BFO – (x) CTO [x=0, 0.1, 0.2 and 0.3] at room temperature

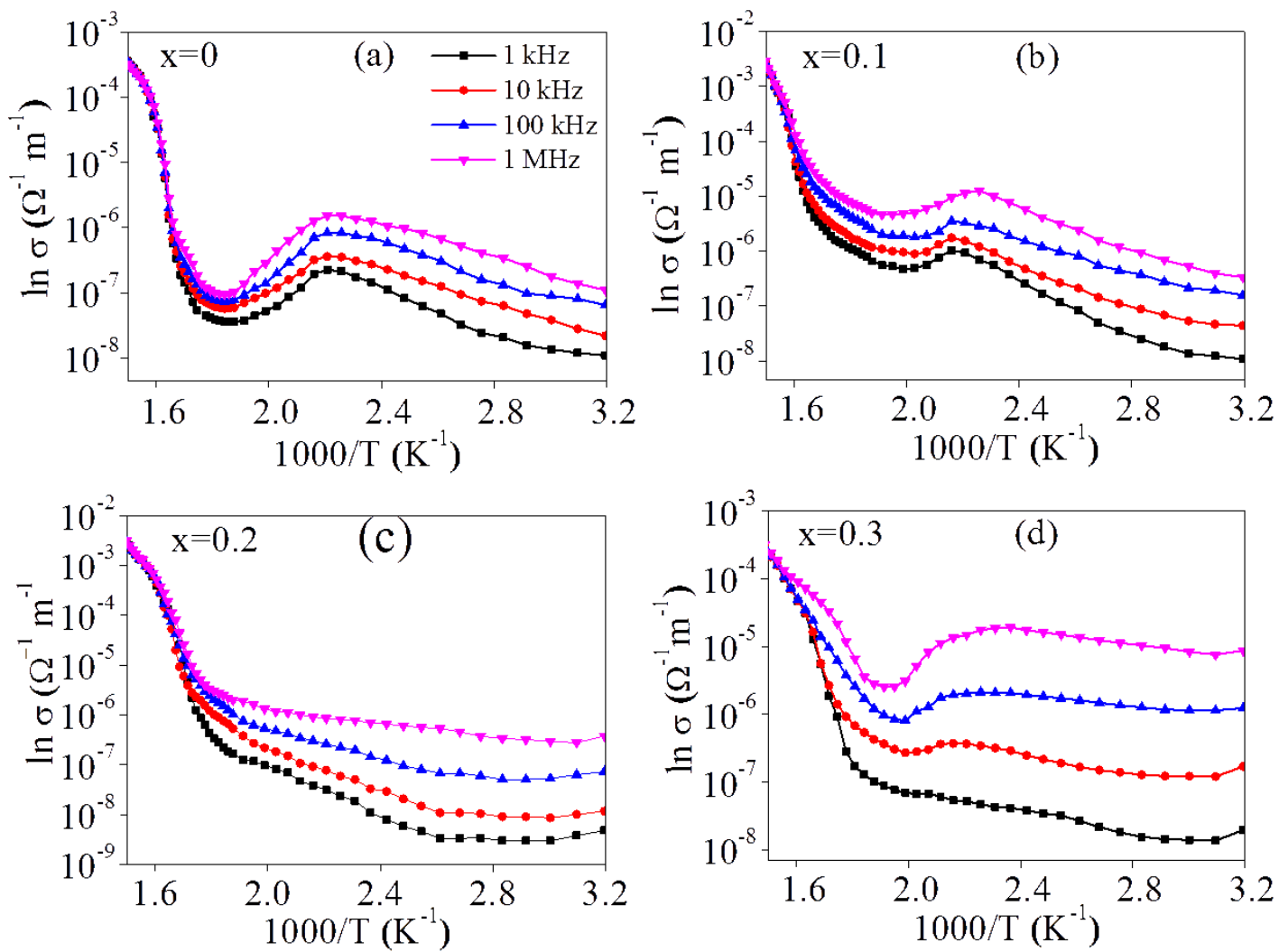


Figure 9

Variation of ac conductivity with inverse of temperature for $(1-x)\text{BFO} - (x)\text{CTO}$ [$x=0, 0.1, 0.2$ and 0.3]

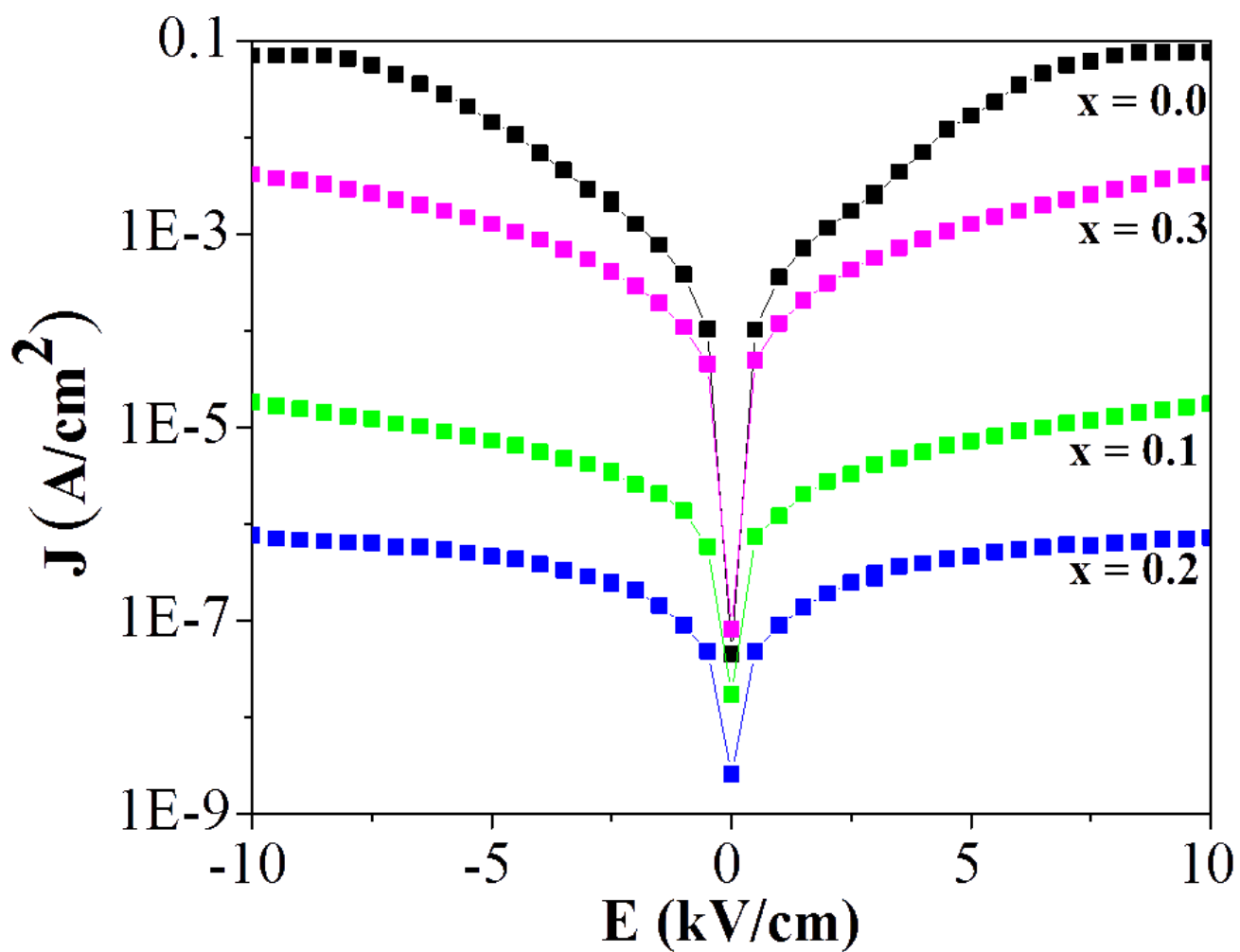


Figure 10

Leakage current densities (J) as a function of electric field (E) for $(1-x)$ BFO – (x) CTO ($x=0, 0.1, 0.2$ and 0.3)

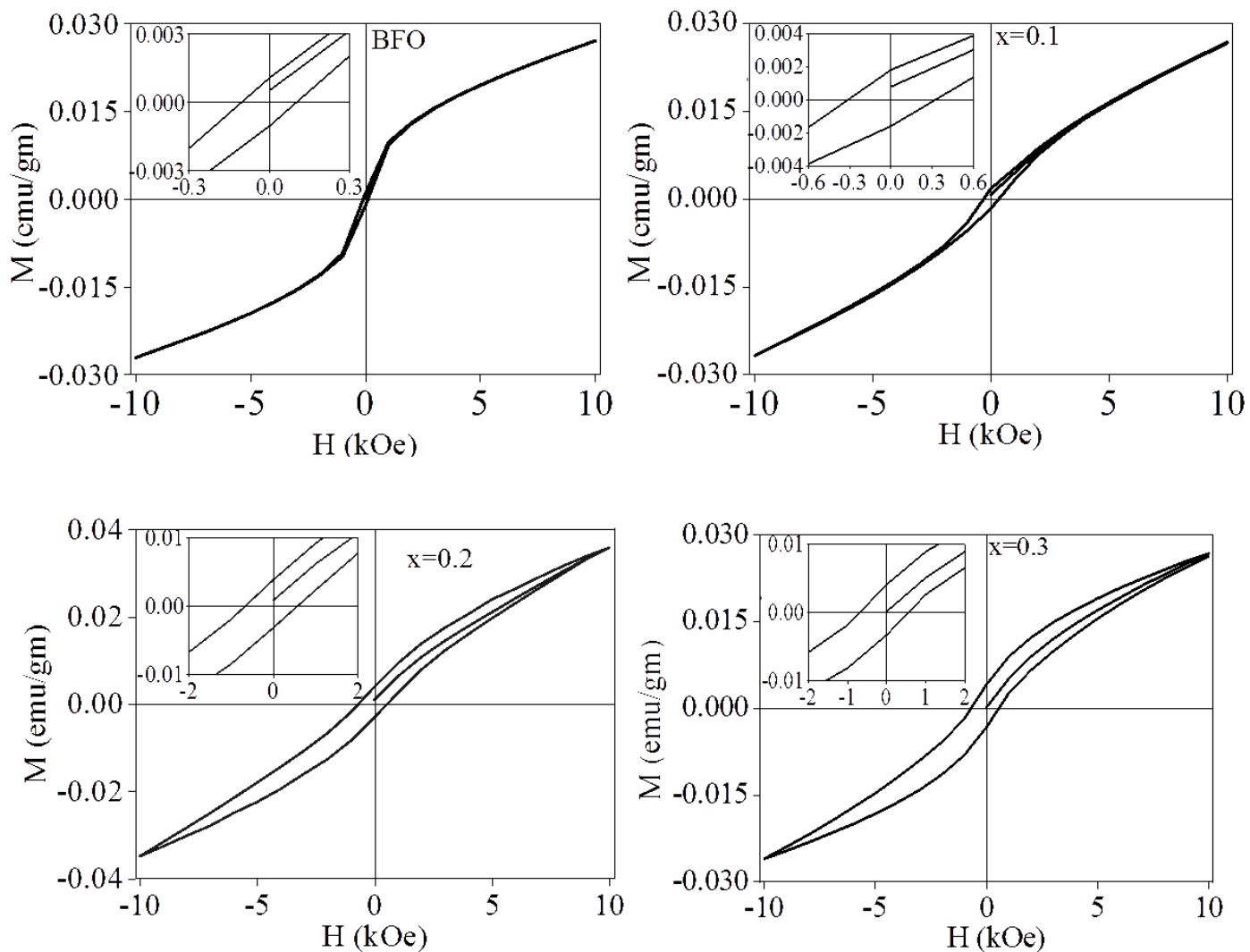


Figure 11

Hysteresis loop for $(1-x)\text{BFO} - x\text{CTO}$ ($x=0, 0.1, 0.2$ and 0.3)

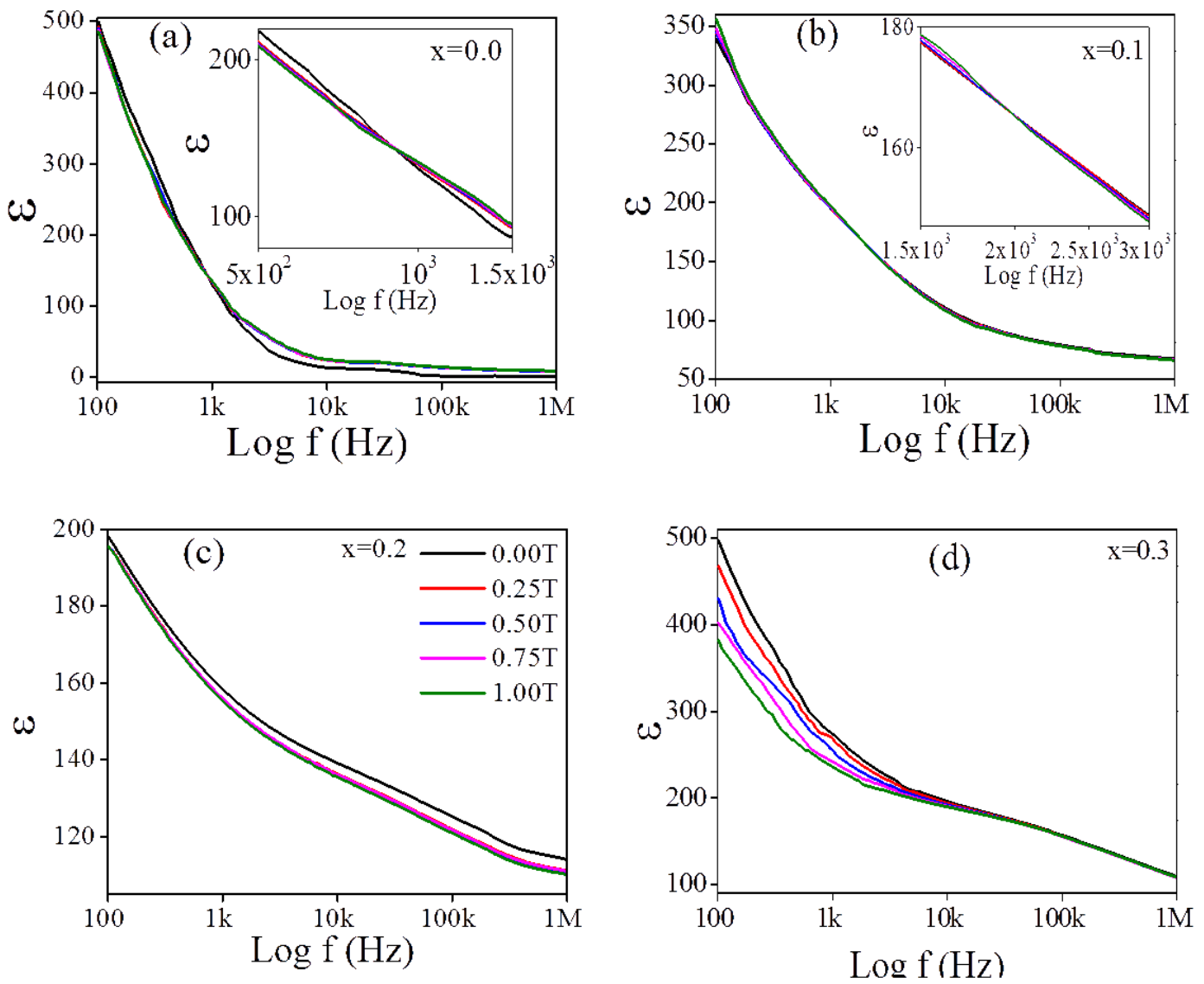


Figure 12

Frequency response of dielectric permittivity at room temperature at different magnetic field (0, 0.25, 0.50, 0.75 and 1 Tesla) for (1-x) BFO – (x) CTO [$x=0, 0.1, 0.2$ and 0.3]

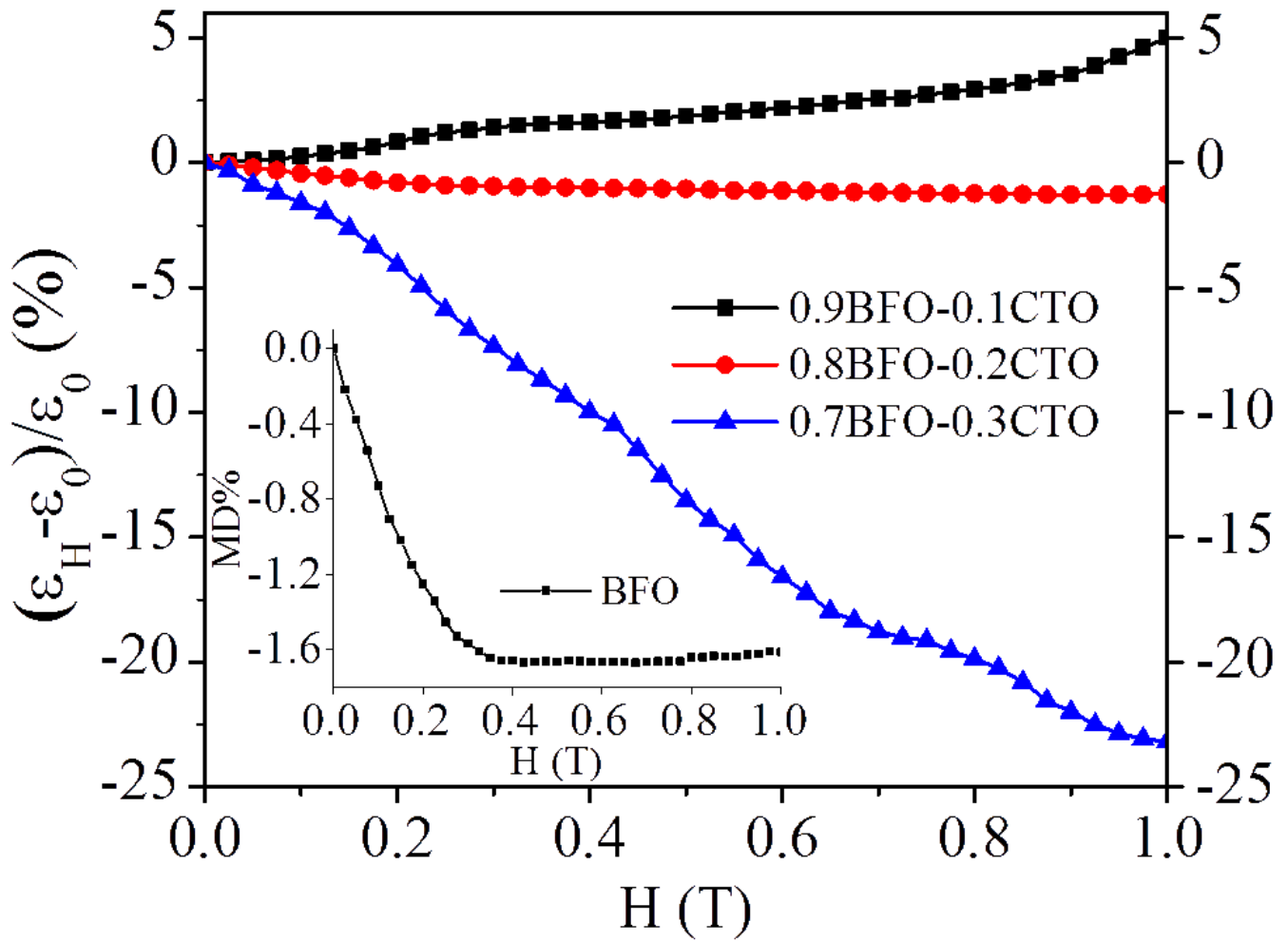


Figure 13

MD% versus magnetic field for (1-x) BFO – (x) CTO [x=0, 0.1, 0.2 and 0.3] (the inset Fig. shows MD plot for BFO)